A study of nonlinearity with spectral element method and linear slip effective medium theory

by

©Meghdad Darijani

A thesis submitted to the School of Graduate Studies in partial fulfillment of the requirements for the degree of

Master of Science (Geophysics)

Department of Earth Sciences

Memorial University of Newfoundland

June 2020

St. John's   Newfoundland

Table of Contents

List of Tables

List of Figures

List of Abbreviations and Symbols

Abbreviations

CAN   Contact acoustic nonlinearity
DAET   Dynamic acousto-elastic testing
EMT   Effective medium theory
NIA   Non-interaction approximation
LS   Linear slip
FDM   Finite difference method
FEM   Finite element method
PSM   Pseudo spectral method
SEM   Spectral element method
TI   Transversely isotropic
VTI   Vertical transverse isotropic
HTI   Horizontal transverse isotropic
TTI   Tilted transverse isotropic
PDE   Partial differential equation
NBC   Neumann boundary condition
GLL   Gauss-Lobatto-Legendre
CFL   Courant-Friedrichs-Lewy

Symbols

σ Stress
ε Strain
λ, μ Lamé's constants
ρ Density
∂ Partial derivative
υ Velocity
b buoyancy
u Displacement
$!$ Factorial
$\nabla \cdot$ Divergence
∇ Gradient
Ω Spatial domain
ξ, η, ζ Reference domain coordinates

ℓ	Lagrange polynomial
δ	Kronecker delta
$\mathcal{J}$	Jacobian
$[u], \Delta u$	Displacement discontinuity
C	Stiffness matrix
S	Compliance matrix
Z	Crack compliance matrix
n	Unit normal
T	Traction

Acknowledgements

I would like to sincerely thank my supervisor, Dr. Alison Malcolm, for her great support during my Master's study. Alison was always kind, welcoming and willing to assist in any way she could throughout the research project. I certainly learned a lot from her, and I am genuinely grateful for her help and guidance during my study.

I would also like to express my great gratitude to Dr. Herurisa Rusmanugroho for his continuous support and help during my study. I am truly thankful for his guidance and encouragement through the process of researching and writing the thesis.

I would also like to greatly thank Dr. Charles Hurich for being in my committee and his help and teaching for the seismic processing course.

I would also highly appreciate Dr. Colin Farquharson for the inversion course during my study.

I would also like to thank my thesis examiners Dr. Kristin M. Poduska and Dr. Michael A. Slawinski for their comments and suggestions.

Last but not least, I wish to say a special thank you to my family and friends, especially some of our research group members for their help and support.

Abstract

In exploration seismology, mapping the Earth's interior structure in more detail is of great interest. The rocks' microstructures, such as cracks, play an essential rule in oil and gas exploration and production. We study elastic nonlinearity because the microstructures are the main reason for this phenomenon. Nonlinearity is also related to the velocity change due to perturbations in the stress filed within the rocks. Many studies have observed the nonlinearity in field data as well as experimental data. However, the exact underlying mechanism of this phenomenon is not well understood. In this study, we provide some numerical examples of wave-perturbed cracked rocks and study the effects of crack aperture size, change of velocity inside crack, and crack orientation on the medium velocity change to better understand this phenomenon. Similar to a few other studies, we study the travel-time delay in a small wave caused by the propagation of a stronger wave. We show that there is a strong dependency between the crack parameters and the travel-time delay.

Chapter 1

Introduction

1.1 Motivation and challenges

Mapping the Earth's interior is of great interest in different areas (e.g., oil and gas, mining, and construction). Our primary interest here is unconventional reservoirs in the context of oil and gas exploration. The rocks' microstructures (e.g., fractures) play an essential role in unconventional reservoirs. The most significant impact of fractures is that they affect the fluid flow through a reservoir. Thus, fracture characterization is vital for enhanced oil recovery from the discovery through the production stage. There are a few ways of fracture characterization such as S-wave splitting (e.g., Vetri et al., 2003), amplitude variation with offset and azimuth (e.g., Rüger, 1998; Rusmanugroho and McMechan, 2010, 2012) and fracture scattering (e.g., Fang et al., 2014; Zheng et al., 2013). In general, all of these methods give some information about the fracture orientation and density. For example, Zheng et al. (2013) propose a method to determine the fracture orientation, spacing and compliance by analyzing the double scattering of waves by fractures. However, we use a different method, with the potential to have more sensitivity to changes in fracture orientations to improve

our understanding of fractured rocks.

In addition to the elastic moduli of the rocks, the strain caused by stress is a contributing factor to the seismic wave velocities because the applied stress can change the rocks' properties and hence the seismic velocities. Velocity perturbations caused by applied load or pressure are a common way to measure nonlinear elasticity in rocks (e.g., Guyer and Johnson, 2009). There is evidence that it is fractures that change during this applied stress. However, it is not clear exactly how they change nor the precise mechanism that causes these changes to result in changes in the velocity (i.e., nonlinear elastic signals). In this study, we use numerical modelling to study these effects. Numerical modelling not only enables us to understand the theory better but also enables us to compare with experimental results. In the following sections of this chapter, we provide a literature review of the critical topics used in this study.

1.2 Nonlinearity

The first topic that we discuss is nonlinearity. Linear elasticity, as opposed to nonlinear elasticity, is based on the two main assumptions: infinitesimal strain and that the stress scales linearly with respect to the strain in Hooke's law. Therefore, the term nonlinearity, in our context, refers to the nonlinear relation between the stress and strain provided by Hooke's law (see, e.g., Helbig, 1998; Johnson and Rasolofosaon, 1996). There are two types of nonlinearity (Helbig, 1998; Rasolofosaon and Yin, 1996): material (physical), and geometric (kinematic) nonlinearity. The material nonlinearity is associated with the intrinsic properties of the material (i.e., microstructures at the grain size or below). It is described by a third rank (or sixth order) elastic stiffness or compliance tensor (Johnson and Rasolofosaon, 1996). The geometrical nonlinearity is due to the full definition of the Lagrangian strain tensor in which the term that

contains the multiplication of displacements' derivatives is neglected in the linear theory by assuming infinitesimal strain (Helbig, 1998). Johnson and Rasolofosaon (1996) and Rasolofosaon and Yin (1996) compare rocks and intact homogeneous materials in their experiments and conclude that the material nonlinearity dominates the geometrical nonlinearity. Guyer and Johnson (1999) explain that the bond system in a material controls the elastic behaviour of that material. The bond system in rocks consists of mechanical defects (e.g., cracks) and grain joints. This is why rocks, which are considered to be nonlinear mesoscopic elastic materials, show a strong nonlinear response compared to atomic elastic materials (e.g., aluminum and glass).

As described above, the nonlinear elasticity theory describes the elastic tensor of material via the stress-strain relation (Hooke's law). Also, the seismic velocities are derived from the components of the elastic tensor. Therefore, we are able to study the nonlinear elasticity through the material velocity changes. Introducing stress causes strain in the medium that affects the mechanical defects and grain joints, which changes the elastic tensor, hence, changing the velocity of the medium. The nonlinearity is induced primarily by the clapping (opening and closing) and frictional contacts of the defects (e.g., Gao et al., 2019). This phenomenon is referred to as contact acoustic nonlinearity (CAN).

Nonlinearity is observed in the field in many studies (e.g., Brenguier et al., 2008; Olivier et al., 2019). Brenguier et al. (2008) show that the seismic velocity of ambient noise changes after an earthquake. There are a few possible mechanisms that could cause these velocity changes as summarized by Xu and Song (2009); these include stress-induced changes of fault zone properties, fault rupture and healing, damage in the shallow crust, and rapid changes in near-surface groundwater or fluid activities in the shallow crust. In Brenguier et al. (2008), they explain that the velocity change is due to damage in the Earth. This conclusion is based on the measured change in the

stress in the subsurface and the observed recovery of the velocities to their pre-stress values modelled as part of a relaxation process after the induced stress.

Similar to Brenguier et al. (2008), Olivier et al. (2019) use seismic ambient noise to measure the velocity change prior to a volcanic eruption. They first observe a velocity increase, which they relate to the closing of the microcracks as the pressure of magma increases. Later they observe that the velocity decreases. They explain that, as the pressure increases, damage in the materials occurs, which weakens the material.

Moving to experimental results, dynamic acousto-elastic testing (DAET) can be used for the study of nonlinearity (e.g., Rivière et al., 2013). In these kinds of experiments, a sample is perturbed by an elastic low-frequency wave, which is called the pump, while a high-frequency wave called the probe is sent into the sample to sense dynamic changes (e.g., velocity changes due to introducing stress or strain) in the sample by the pump (e.g., Haupert et al., 2019). A similar approach is used to capture the nonlinearity in the experiments that we follow most closely (Gallot et al., 2015; TenCate et al., 2016).

TenCate et al. (2016) show the effect of crack orientation on the nonlinear interaction of P- and S-waves. In their experiments, the S-wave pump perturbs the cracked medium, and the P-wave probe senses the perturbation by changes in its arrival time in a setup similar to DAET. These experiments show that the nonlinearity is a feature of the rocks (as mentioned above, when discussing nonlinear mesoscopic materials). Also, when the particle motions of the S-wave are parallel to the bedding planes, the travel-time perturbation of the probe signal is smaller than when the particle motions are perpendicular to the bedding plane. In other words, the former setup results in a smaller velocity change in the medium. This explanation can be used to indicate the direction of fractures in a reservoir.

Having discussed the nonlinear theory, we now need to introduce the effective

medium theory and its applications. This is because we have many cracks in the medium, and we need to know how to compute a change in velocity from a change in their properties. In the following section, we introduce the theory and why we need such a theory as well as our choice of method.

1.3   Effective medium theory

Fractures are a crucial part of rocks in the study of unconventional hydrocarbon reservoirs. Although their volume might be a small portion of the rock, they control the porosity and permeability of that rock. The crucial parameters of fractures that control the porosity and permeability are the fracture density, the fracture orientation and the fracture aperture (e.g., Ali, 2011, p. 11). In addition to these properties, the existence of fractures changes the elastic properties of a rock, hence, changes the elastic tensor describing that rock. Understanding these effects is important to better understand the properties of the Earth. Wave propagation in the subsurface with a set of fractures produces velocity anisotropy, which we can use for fracture characterization (Guo et al., 2019). Since the size of the fractures is extremely small compared to the seismic wavelength, it is difficult or even almost impossible to detect an individual fracture's effect on the seismic response. This is why we use an effective medium theory (EMT) to sense the behaviour of an equivalent anisotropic averaged (also known as up-scaled) medium that represents the fractured medium.

As mentioned above, the existence of cracks contributes to the elastic stiffness tensor describing the medium. One can divide this contribution into two parts: individual contribution of cracks and the crack interactions with each other. The T-matrix method (Jakobsen et al., 2003a,b) can be used when the crack density is not small. This theory takes into account the interactions of points located in different cracks

7

(shielding) as well as the interaction between all points in a single crack (amplification), which provides physically-based predictions (Hu and McMechan, 2009).

The non-interaction approximation (NIA) is used to obtain the effective stiffness tensor of a fractured rock, assuming these cracks do not interact, which simplifies the calculations. In our case, where the crack density is very small, the contribution of cracks' interactions is negligible (e.g., Hu and McMechan, 2009). Most of the popular methods of obtaining effective elastic tensors use the NIA (see, e.g., Zhao et al., 2016).

The calculation of the effective stiffness tensor for a fractured medium within the NIA can be classified in two ways: direct, and indirect (e.g., Hu and McMechan, 2009; Zhao, 2014, p. 22). In the direct methods, the stiffness tensor is estimated directly. In contrast, in the indirect methods, first, we calculate the effective compliance tensor, from which the effective stiffness tensor can be obtained by inverting the compliance tensor. There are a few effective medium theories (see, e.g., Hu and McMechan, 2009; Zhao, 2014, p. 22) that we can use. The two most popular and widely used methods of NIA are (Fang et al., 2017) the Hudson's method of averaging (Hudson, 1980, 1994, 1981) and the averaging method based on the linear slip (LS) theory of Schoenberg (Schoenberg, 1980; Schoenberg and Douma, 1988; Schoenberg and Sayers, 1995).

Using scattering theory, Hudson (1980) and Hudson (1981) provide the effective stiffness tensor of an isotropic medium with penny-shaped ellipsoidal cracks embedded in the medium. Schoenberg (1980) and Schoenberg and Douma (1988) provide the effective compliance tensor of an isotropic medium embedded with fractures that are modelled as thin layers (i.e., planes of weakness) with LS boundary conditions. Hudson (1980) represents a direct method for estimating the stiffness tensor, while Schoenberg (1980) represents an indirect method for estimating the compliance tensor.

Grechka and Kachanov (2006) show that both methods predict a similar elastic response when the crack density is small. The accuracy of Hudson's theory decreases

when the crack density is large, but Schoenberg's theory remains sufficiently accurate (Grechka and Kachanov, 2006). However, one should be careful not to use NIA based (e.g., Schoenberg's theory) methods in high crack density media. Although these methods might provide good predictions, they are un-physical because they break the dilute crack assumption of the NIA in most Earth materials (Hu and McMechan, 2009).

Considering the above discussions, we choose Schoenberg's EMT for our study because it uses the displacement discontinuity in the formulation of the method, which is directly related to the clapping of the cracks, which we are going to investigate in this study because we believe this clapping to be a key component of the nonlinear response.

Using nonlinear theory and effective medium theory together can help us better understand fractured media. In addition to these theories, we need a tool to use these methods together. Numerical modelling is the tool that is needed for our goal to study fractured media. In the following section, we talk about the numerical modelling and why we need such a tool as well as our choice of method of numerical modelling.

1.4   Numerical modelling

Numerical modelling techniques allow us to study the details of a theory helping us decode the complicated mechanism behind that theory, which is not always possible in experimental studies. In this study, we use numerical modelling to study wave propagation. There are three main categories for seismic wave propagation modelling (e.g., Carcione et al., 2002; Wang, 2015, p. 36): first, ray-tracing methods, which are based on the Eikonal and transport equations. Second, the integral equation methods, in which the wavefield is the superposition of waves originating from a point source

using Huygens principle and using Green's functions to set up an integral system of equations. The third and the last methods are the direct or wave equation methods in which the Newtonian mechanics and elastic (or acoustic) theory are used to solve the wave equation on a discretized medium on a certain number of mesh points. Finite difference method (FDM), finite element method (FEM), pseudo spectral method (PSM) and spectral element method (SEM) are some of the methods in this category. In FDM, the Taylor expansion is used to solve the wave equation on structured grid points. There are regular FDM (e.g., Kelly et al., 1976) and staggered grid FDM (e.g., Graves, 1996; Virieux, 1986). FEM is based on a weak or a variational form of the wave equation and uses unstructured grid points allowing us to handle more complex geometries than FDM. FEM is applied to the study of wave propagation in sedimentary basins (e.g., Bao et al., 1998), although it is not as popular as FDM in seismic modelling. PSM is a higher-order method that allows us to get the required accuracy using a few grid points per wavelength. It is based on polynomial (e.g., Chebyshev or Legendre) and harmonic (i.e., Fourier) basis functions and similar to FDM is difficult to set up for complex geometries. This method is commonly used to study wave propagation in the whole earth (e.g., Wang et al., 2001). The SEM works similar to the FEM. It combines the accuracy of PSM with the flexibility of FEM, which allows us to get better results than the other methods (e.g., Komatitsch and Tromp, 1999; Komatitsch et al., 1999).

We use the SEM to do our simulations, and give details on the method in the following chapter. Now that we have all the tools needed, we can study fractured media and increase our understanding of the nonlinear theory.

1.5 Similar studies and thesis outline

There are some numerical modelling studies that help us better understand the non-linearity phenomenon (e.g., Guo et al., 2019; Pecorari, 2015). Both of these studies investigate the nonlinearity through the clapping cracks using different approaches. However, our approach is different and is similar to the study done by Rusmanugroho et al. (2020) in which they mimic the experiments done by TenCate et al. (2016) as we do in this study with a different approach. They observe a similar trend with TenCate et al. (2016) in the travel-time delay in a cracked medium while comparing different cracks orientations. There are three significant differences between Rusmanugroho et al. (2020) and our study. First, we use SEM in 2D, and they use FDM in 3D. Second, we use the linear wave equation, but they use the nonlinear wave equation for wave propagation modelling. The last difference is that the linear slip is implemented in the FDM code in their study, while in our study, we use a different method as is discussed later in the thesis. The difference is in how we calculate the displacement discontinuity. Aside from the differences, both studies give insights about the relation between cracks' properties and the P-wave velocity change (or P-wave travel-time delay) in a perturbed cracked medium, which helps us to better understand the microstructures in the rock.

In the following chapter, Chapter 2, we provide the theories that are used, such as wave propagation within an elastic media, spectral element modelling, and the linear slip effective medium theory. After that, in Chapter 3, we discuss a few methods of effective P-wave velocity calculations and introduce our procedure for calculating the travel-time delays. We then present the results of our modelling in Chapter 4. Discussion, conclusions and future work are presented in Chapter 5. In the end, some derivations and code validations are provided in appendices A and B, respectively.

Chapter 2

Methodology

In this chapter, first, we provide the formulation of seismic wave propagation in three spatial dimensions and discuss the formulation of Hooke's law and its properties for an isotropic medium. Next, we explain the numerical modelling techniques and provide some details of the spectral element method. Then, we introduce the linear slip effective medium theory and its formulation in detail. After that, we provide the two-dimensional formulations of the effective medium theory from our generalized three-dimensional problem. In the end, we provide more details of the linear slip through the crack compliances and then show how to average a quantity on a surface.

2.1 Wave Equation

Before introducing the equations that describe seismic wave propagation in the general case, we will briefly discuss stress and strain. The stress tensor (σ_{ij}), as well as the strain tensor (ε_{ij}), has nine components in which each component acts in one direction and on one plane. The stress and strain for an elastic medium are related by Hooke's

law,

$$\sigma_{ij} = c_{ijkl}\varepsilon_{kl}, \quad (i,j,k,l=1,2,3), \tag{2.1}$$

where c_{ijkl} is the stiffness tensor containing the constant elastic moduli describing the properties of the medium with 81 components. We use the summation convention where we sum from 1-3 over repeated indices. Stress and strain are symmetric tensors which means $\sigma_{ij} = \sigma_{ji}$ and $\varepsilon_{ij} = \varepsilon_{ji}$ which drops from 9 to 6 independent components for each tensor (the number of equations in (2.1) decreases from 9 to 6 independent equations),

$$\begin{bmatrix} \sigma_{11} & \sigma_{12} & \sigma_{13} \\ \sigma_{21} & \sigma_{22} & \sigma_{23} \\ \sigma_{31} & \sigma_{32} & \sigma_{33} \end{bmatrix} \longrightarrow \begin{bmatrix} \sigma_1 & \sigma_6 & \sigma_5 \\ \sigma_6 & \sigma_2 & \sigma_4 \\ \sigma_5 & \sigma_4 & \sigma_3 \end{bmatrix}, \quad \begin{bmatrix} \varepsilon_{11} & \varepsilon_{12} & \varepsilon_{13} \\ \varepsilon_{21} & \varepsilon_{22} & \varepsilon_{23} \\ \varepsilon_{31} & \varepsilon_{32} & \varepsilon_{33} \end{bmatrix} \longrightarrow \begin{bmatrix} \varepsilon_1 & \frac{1}{2}\varepsilon_6 & \frac{1}{2}\varepsilon_5 \\ \frac{1}{2}\varepsilon_6 & \varepsilon_2 & \frac{1}{2}\varepsilon_4 \\ \frac{1}{2}\varepsilon_5 & \frac{1}{2}\varepsilon_4 & \varepsilon_3 \end{bmatrix}. \tag{2.2}$$

As mentioned above, the stress and strain tensors are symmetric, therefore $c_{ijkl} = c_{jikl}$ and $c_{ijkl} = c_{ijlk}$, which reduces the number of independent components to 36. The stiffness tensor can be represented by a 6×6 matrix $(c_{\alpha\beta})$ with Voigt notation (Thomsen, 1986),

$$\begin{array}{cccccccc} ij & kl & : & 11 & 22 & 33 & 23,32 & 13,31 & 12,21 \\ \Downarrow & \Downarrow & & \Downarrow & \Downarrow & \Downarrow & \Downarrow & \Downarrow & \Downarrow \\ \alpha & \beta & & 1 & 2 & 3 & 4 & 5 & 6 \end{array}. \tag{2.3}$$

13

The stiffness matrix components are (Nye, 1985),

$$
\begin{aligned}
c_{ijkl} &= c_{\alpha\beta} \quad \text{when } \alpha \text{ and } \beta \text{ are } 1, 2 \text{ or } 3, \\
2c_{ijkl} &= c_{\alpha\beta} \quad \text{when one either } \alpha \text{ or } \beta \text{ are } 4, 5 \text{ or } 6, \\
4c_{ijkl} &= c_{\alpha\beta} \quad \text{when both } \alpha \text{ and } \beta \text{ are } 4, 5 \text{ or } 6.
\end{aligned} \tag{2.4}
$$

Based on the strain energy definition we have $c_{ijkl} = c_{klij}$ (see, e.g., Slawinski, 2010, pp. 106-107), and the number of independent components in an anisotropic medium (general case) is 21 elastic constants (Stein and Wysession, 2009). The number of independent elastic constants is reduced more with more symmetry of the medium.

The most symmetric medium (i.e., symmetry in all directions) is an isotropic medium in which the material has only two independent elastic moduli, called Lamé's constants, λ and μ. μ is the shear modulus, which is a measure of resistance to shear stress, and λ has no apparent physical meaning. There is another symmetry called transversely isotropic (TI) in which a medium has a rotational-symmetry axis along one direction. Symmetry axes in TI medium can be vertical (VTI), horizontal (HTI) and tilted (TTI) in which tilted means that the symmetry axis is not along any of the three basic coordinate axes. In VTI or HTI medium, we have twelve elastic constants in which five of them are independent. There are also five independent elastic constants in a TTI medium (Ikelle and Amundsen, 2005; Slawinski, 2010).

As mentioned above, in the general case (anisotropic medium) there are 36 non-zero elastic constants with 21 independent components; for the isotropic case there are 12 non-zero elastic constants with only two independent components,

$$
\begin{cases}
\lambda = c_{11} - 2c_{44} \\
\mu = c_{44}
\end{cases}, \tag{2.5}
$$

14

and we have the following elastic tensor for an isotropic medium,

$$\begin{bmatrix} \lambda + 2\mu & \lambda & \lambda & 0 & 0 & 0 \\ \lambda & \lambda + 2\mu & \lambda & 0 & 0 & 0 \\ \lambda & \lambda & \lambda + 2\mu & 0 & 0 & 0 \\ 0 & 0 & 0 & \mu & 0 & 0 \\ 0 & 0 & 0 & 0 & \mu & 0 \\ 0 & 0 & 0 & 0 & 0 & \mu \end{bmatrix}. \tag{2.6}$$

The stress tensor describes the forces that act on a deformable continuous medium. Now that we have the stress and the strain relation, we introduce the equation of motion, which relates the stress to the displacement (or the variation in the displacement described by the strain tensor).

The first-order system of partial differential equations (PDEs) for the equations of dynamic elasticity, which is called the velocity-stress formulation is (see, e.g., Tessmer, 1995),

$$\begin{aligned} \rho \dot{v}_x &= \frac{\partial \sigma_{xx}}{\partial x} + \frac{\partial \sigma_{xy}}{\partial y} + \frac{\partial \sigma_{xz}}{\partial z} + f_x, \\ \rho \dot{v}_y &= \frac{\partial \sigma_{xy}}{\partial x} + \frac{\partial \sigma_{yy}}{\partial y} + \frac{\partial \sigma_{yz}}{\partial z} + f_y, \\ \rho \dot{v}_z &= \frac{\partial \sigma_{xz}}{\partial x} + \frac{\partial \sigma_{yz}}{\partial y} + \frac{\partial \sigma_{zz}}{\partial z} + f_z, \end{aligned} \tag{2.7}$$

where ρ is the density, f_i is the source, and v_i is the velocity. A dot above a variable denotes differentiation with respect to time.

To solve Equation (2.7), we need to relate σ and v using Equation (2.1) by defining the time derivative of the strain tensor,

$$\dot{\varepsilon}_{ij} = \frac{1}{2}\left(\frac{\partial v_i}{\partial x_j} + \frac{\partial v_j}{\partial x_i}\right). \tag{2.8}$$

15

For an isotropic medium, using Equations (2.1), (2.7) and (2.8) we have,

$$
\begin{aligned}
\dot{v}_x &= b\Big(\frac{\partial \sigma_{xx}}{\partial x} + \frac{\partial \sigma_{xy}}{\partial y} + \frac{\partial \sigma_{xz}}{\partial z} + f_x\Big), \\
\dot{v}_y &= b\Big(\frac{\partial \sigma_{xy}}{\partial x} + \frac{\partial \sigma_{yy}}{\partial y} + \frac{\partial \sigma_{yz}}{\partial z} + f_y\Big), \\
\dot{v}_z &= b\Big(\frac{\partial \sigma_{xz}}{\partial x} + \frac{\partial \sigma_{yz}}{\partial y} + \frac{\partial \sigma_{zz}}{\partial z} + f_z\Big),
\end{aligned}
\tag{2.9}
$$

and

$$
\begin{aligned}
\dot{\sigma}_{xx} &= (\lambda + 2\mu)\Big(\frac{\partial v_x}{\partial x}\Big) + \lambda\Big(\frac{\partial v_y}{\partial y} + \frac{\partial v_z}{\partial z}\Big), \\
\dot{\sigma}_{yy} &= (\lambda + 2\mu)\Big(\frac{\partial v_y}{\partial y}\Big) + \lambda\Big(\frac{\partial v_x}{\partial x} + \frac{\partial v_z}{\partial z}\Big), \\
\dot{\sigma}_{zz} &= (\lambda + 2\mu)\Big(\frac{\partial v_z}{\partial z}\Big) + \lambda\Big(\frac{\partial v_x}{\partial x} + \frac{\partial v_y}{\partial y}\Big), \\
\dot{\sigma}_{xy} &= \mu\Big(\frac{\partial v_x}{\partial y} + \frac{\partial v_y}{\partial x}\Big), \\
\dot{\sigma}_{xz} &= \mu\Big(\frac{\partial v_x}{\partial z} + \frac{\partial v_z}{\partial x}\Big), \\
\dot{\sigma}_{yz} &= \mu\Big(\frac{\partial v_y}{\partial z} + \frac{\partial v_z}{\partial y}\Big),
\end{aligned}
\tag{2.10}
$$

where $b = 1/\rho$ is the buoyancy.

So far, we have formulated the wave equation for seismic wave propagation in an isotropic medium in three spatial dimensions, which is the first step of our elastic modelling problem. Having this formulation, we introduce a variety of numerical modelling techniques to numerically solve the wave equation in the following section.

2.2 Numerical Methods

PDEs such as the elastic wave equation described in the previous section, are known for describing many natural laws. Since the PDEs in which we are usually interested do not have exact solutions, we seek approximate solutions with numerical methods such as the FDM, the FEM and the SEM. In this section, we are going to introduce these methods focusing on the formulation of the SEM method.

FDM needs a large number of grid points to achieve sufficient accuracy for our

purposes. Also, more complex geometries are more challenging to handle in the FDM than in the FEM and the SEM, even with a large number of grid points. This is because we use structured meshes in the FDM but unstructured meshes in the FEM and SEM. Because the SEM uses high-order basis functions, it gives more accurate results than the FEM when both have the same number of grid points (Komatitsch et al., 1999). This means that SEM maintains the flexibility of FEM with improved accuracy (Komatitsch and Tromp, 2002).

2.2.1 FDM

The first numerical method that we are going to describe is the FDM. In the FDM, the derivatives at each grid point are calculated from the neighbouring grid points based on Taylor's theorem. Based on the PDEs' properties, one divides the spatial and/or temporal domain into a finite mesh (grids), then by applying Taylor's theorem and replacing the partial derivatives by their approximations, we construct an approximate solution to our PDE. The 1D $(n-1)$-st order Taylor's expansion of u at x_0 (Causon and Mingham, 2010) is,

$$u(x_0 + h) = u(x_0) + hu_x(x_0) + h^2 \frac{u_{xx}(x_0)}{2!} + ... + h^{n-1} \frac{u_{n-1}(x_0)}{(n-1)!} + O(h^n), \quad (2.11)$$

where $u_n(x_0)$ is the n-th derivative with respect to x at $x = x_0$, h is the grid spacing in FDM and $O(h^n)$ is the error term in the Taylor approximation. From (2.11), we derive the first order forward (from x_0 to $x_0 + h$) finite difference approximation,

$$u_x(x_0) \approx \frac{u(x_0 + h) - u(x_0)}{h} := D_x u. \quad (2.12)$$

A similar approach is then used to compute higher-order derivatives.

17

2.2.2 FEM and SEM

The SEM and the FEM are based on the weak formulation (i.e., PDE is transformed into an integral equation) of the wave equation, Equation (2.7). In traditional FEM, we use the same low-degree polynomials to describe the geometry of an element and to represent functions, such as the displacement field and test function (a time-independent generic weighting function) on an element. In SEM, we also use a low-degree polynomial to describe the shape of an element, but a higher-degree polynomial to represent functions on those elements (Komatitsch and Tromp, 2002).

Equation (2.7), the wave equation, can be written in the following compact form,

$$
\begin{aligned}
\rho \frac{\partial^2 u_i}{\partial t} &= \frac{\partial \sigma_{ij}}{\partial j} + f_i, \\
\rho \ddot{u}_i &= \sigma_{ij,j} + f_i, \quad (i \text{ and } j = 1, 2, 3), \\
\rho \ddot{\mathbf{u}} &= \nabla \cdot \boldsymbol{\sigma} + \mathbf{f},
\end{aligned}
\tag{2.13}
$$

where the comma denotes a spatial derivative in the direction given index following the comma, and the bold symbol denotes a vector (here three dimensional). The stress is also related to the displacement gradient by Hooke's law,

$$
\boldsymbol{\sigma}(\nabla \mathbf{u}) = c(\mathbf{x}) : \nabla \mathbf{u}(\mathbf{x}, t),
\tag{2.14}
$$

where the colon represents the contracted product of two tensors, such that $\mathbf{c}=\mathbf{a}{:}\mathbf{b}$ is equivalent to $c_{ij} = a_{ijkl}b_{kl}$ (see, e.g., Komatitsch, 1997; Komatitsch and Vilotte, 1998). Therefore, Equations (2.1) and (2.14) are equivalent. The former is written in a component form using the index summation notation, and the latter is written in tensor form using the double dot product (double contraction over the last two indices of the first tensor and the first two indices of the second tensor) after using time-integrated of Equation (2.8).

As mentioned above, the SEM, like the FEM, is based on an integral or weak formulation. In order to get the weak formulation, we multiply the wave equation (the last equation in Equation (2.13)) with an arbitrary time-independent vector $\mathbf{w}$, called the test function, which has to be smooth, meaning that it has to have at least one continuous derivative, and then integrate over the spatial domain or volume, Ω, so,

$$\int_\Omega \mathbf{w}\, \rho\, \ddot{\mathbf{u}}\, d\mathbf{x} = \int_\Omega \mathbf{w}\, \nabla \cdot \boldsymbol{\sigma}\, d\mathbf{x} + \int_\Omega \mathbf{w}\, \mathbf{f}\, d\mathbf{x}. \tag{2.15}$$

Using integration by parts and denoting the boundary of Ω by Γ, we obtain,

$$\int_\Omega \mathbf{w}\, \rho\, \ddot{\mathbf{u}}\, d\mathbf{x} = \int_\Gamma \mathbf{w}\, \nabla \cdot \boldsymbol{\sigma}\, d\mathbf{x} - \int_\Omega \nabla \mathbf{w}\, \boldsymbol{\sigma}\, d\mathbf{x} + \int_\Omega \mathbf{w}\, \mathbf{f}\, d\mathbf{x}. \tag{2.16}$$

One can apply different boundary conditions and source functions in (2.16) (see, e.g., Komatitsch and Tromp, 1999, 2002). Considering continuous fields, here for the sake of simplicity we apply a free surface boundary condition, which is also called a Neumann boundary condition (NBC) in which the stress is zero at the boundaries (e.g., Martin et al., 2008; Meza-Fajardo et al., 2008; Schuberth, 2003); therefore we have,

$$\int_\Omega \mathbf{w}\, \rho\, \ddot{\mathbf{u}}\, d\mathbf{x} + \int_\Omega \nabla \mathbf{w}\, \boldsymbol{\sigma}\, d\mathbf{x} = \int_\Omega \mathbf{w}\, \mathbf{f}\, d\mathbf{x}. \tag{2.17}$$

Now we need to discretize the physical domain Ω into n_e elements, Ω_e, which are non-overlapping subdomains that cover the entire domain. We perform Equation (2.17) on each element of the domain independently,

$$\int_{\Omega^e} \mathbf{w}\, \rho\, \ddot{\mathbf{u}}\, d\mathbf{x} = - \int_{\Omega^e} \nabla \mathbf{w}\, \boldsymbol{\sigma}\, d\mathbf{x} + \int_{\Omega^e} \mathbf{w}\, \mathbf{f}\, d\mathbf{x}, \tag{2.18}$$

where $e = 1, 2, ..., n_e$.

We solve the problem on the elements; therefore, we need to map each element from

19

the global or physical coordinate into the local or reference coordinate. The general mapping function between the Cartesian points $\mathbf{x} = (x, y, z)$ within a hexahedral element Ω_e and the reference cube points $\boldsymbol{\xi} = (\xi, \eta, \zeta)$ is of the form,

$$\mathbf{x}^e(\boldsymbol{\xi}) = \sum_{a=1}^{n_a} N_a(\boldsymbol{\xi})\mathbf{x}_a^e, \tag{2.19}$$

where the reference domain is a standard interval $\Lambda = [-1, 1]$ for the vector $\boldsymbol{\xi}$. The shape functions N_a determine the geometry of the element and are n_d products (n_d is the number of dimensions) of Lagrangian polynomials. The degree of Lagrangian polynomials is usually 1 ($= 2$ nodes per dimension) or 2 ($= 3$ nodes per dimension), depending on the model. The $n + 1$ Lagrange polynomials of degree n are defined in terms of $n + 1$ control points, ξ_i, as,

$$\ell_i^n(\xi) = \prod_{\substack{j=0 \\ j \neq i}}^{n} \frac{\xi - \xi_j}{\xi_i - \xi_j}, \tag{2.20}$$

where the control points are in the interval Λ. The definition of Lagrange polynomials (Equation (2.20)) has an important characteristic; each polynomial ℓ_i is one at the ξ_i and 0 at all other nodes of the element,

$$\ell_i^n(\xi_j) = \delta_{ij}, \tag{2.21}$$

where δ_{ij} is the Kronecker delta.

Here we define the Jacobian ($\mathcal{J}$), which is used for the transformation of integrals from the global coordinate system to the local coordinate system as,

$$dx\, dy\, dz = \mathcal{J}^e\, d\xi\, d\eta\, d\zeta. \tag{2.22}$$

The 3×3 Jacobi matrix (J) and its determinant are defined as,

$$
\begin{aligned}
\mathsf{J}^e &= \frac{\partial \mathbf{x}^e(\boldsymbol{\xi})}{\partial(\boldsymbol{\xi})}, \\
&= \sum_{a=1}^{n_a} \frac{\partial N_a(\boldsymbol{\xi})}{\partial(\boldsymbol{\xi})} \mathbf{x}_a^e, \\
\mathcal{J}^e &= \mathbf{det}\, \mathsf{J}^e, \\
&= \begin{vmatrix}
\dfrac{\partial x(\boldsymbol{\xi})}{\partial(\xi)} & \dfrac{\partial x(\boldsymbol{\xi})}{\partial(\eta)} & \dfrac{\partial x(\boldsymbol{\xi})}{\partial(\zeta)} \\[2mm]
\dfrac{\partial y(\boldsymbol{\xi})}{\partial(\xi)} & \dfrac{\partial y(\boldsymbol{\xi})}{\partial(\eta)} & \dfrac{\partial y(\boldsymbol{\xi})}{\partial(\zeta)} \\[2mm]
\dfrac{\partial z(\boldsymbol{\xi})}{\partial(\xi)} & \dfrac{\partial z(\boldsymbol{\xi})}{\partial(\eta)} & \dfrac{\partial z(\boldsymbol{\xi})}{\partial(\zeta)}
\end{vmatrix}.
\end{aligned}
\tag{2.23}
$$

In what follows, we omit the superscript e, which denotes an element.

To solve the problem on each mesh point, we approximate the functions of Equation (2.18) by discrete functions using an interpolation scheme on a few discrete points on each element. Therefore, we need several functions F (e.g., F can be displacement or a test function) at the grid points in each element. For interpolation, we use the Lagrange polynomials (usually of degree 4 to 10), which are defined on the Gauss-Lobatto-Legendre (GLL) points which are the roots of $(1 - \xi^2)P_n'(\xi) = 0$, where $P_n'(\xi)$ is the derivative of the Legendre polynomials of degree n. Functions F on an element are interpolated via,

$$
\begin{aligned}
F(\mathbf{x}(\boldsymbol{\xi})) &\approx \sum_{i,j,k=0}^{n_i,n_j,n_k} F(\mathbf{x}(\xi_i, \eta_j, \zeta_k))\ell_i(\xi)\ell_j(\eta)\ell_k(\zeta), \\
&\approx \sum_{i,j,k=0}^{n_i,n_j,n_k} F^{ijk}\ell_i(\xi)\ell_j(\eta)\ell_k(\zeta),
\end{aligned}
\tag{2.24}
$$

where F^{ijk} is the value of the function F at the GLL point $\mathbf{x}(\xi_i, \eta_j, \zeta_k)$ and n_i denotes the polynomial degree. We have omitted the superscript n on the Lagrange polynomials. Using the definition of the gradient of a function, $\nabla F = \sum_{l=1}^{3} \hat{\mathbf{x}}_l \partial_l F$, evaluated

21

at GLL point $\mathbf{x}(\xi_\alpha, \eta_\beta, \zeta_\gamma)$ we have,

$$
\begin{aligned}
\nabla F(\mathbf{x}(\xi_\alpha, \eta_\beta, \zeta_\gamma)) \approx \sum_{l=1}^{3} \hat{\mathbf{x}}_l \Bigg[& (\partial_l \xi)^{\alpha\beta\gamma} \sum_{i=0}^{n_i} F^{i\beta\gamma} \, \ell'_i(\xi_\alpha) \\
& + (\partial_l \eta)^{\alpha\beta\gamma} \sum_{j=0}^{n_j} F^{\alpha j \gamma} \, \ell'_j(\eta_\beta) \\
& + (\partial_l \zeta)^{\alpha\beta\gamma} \sum_{k=0}^{n_k} F^{\alpha\beta k} \, \ell'_k(\zeta_\gamma) \Bigg],
\end{aligned}
\tag{2.25}
$$

where $\hat{\mathbf{x}}_l$ denote unit vectors along the l-coordinate axis and, prime denotes derivatives of the Lagrange polynomials. The matrix $\partial\boldsymbol{\xi}/\partial\mathbf{x}$ is obtained by inverting the Jacobian matrix defined in Equation (2.23).

Integration over an element is thus transformed into a finite weighted sum using GLL quadrature of integration by,

$$
\begin{aligned}
\int_\Lambda F(\mathbf{x}) d\mathbf{x} &= \int_{-1}^{1} \int_{-1}^{1} \int_{-1}^{1} F(\mathbf{x}(\xi, \eta, \zeta)) \, J(\xi, \eta, \zeta) \, d\xi \, d\eta \, d\zeta \\
&\approx \sum_{i,j,k=0}^{n_i, n_j, n_k} \boldsymbol{w}_i \, \boldsymbol{w}_j \, \boldsymbol{w}_k \, F^{ijk} \, J^{ijk},
\end{aligned}
\tag{2.26}
$$

where $\boldsymbol{w}_i$ are positive GLL quadrature weights.

We expand the displacement field $\mathbf{u}$ and the test vector $\mathbf{w}$ in terms of Lagrange polynomials using Equation (2.24),

$$
\mathbf{u}(\mathbf{x}(\xi, \eta, \zeta), t) \approx \sum_{l=1}^{3} \hat{\mathbf{x}}_l \sum_{i,j,k=0}^{n_i, n_j, n_k} u_l^{ijk} \ell_i(\xi) \ell_j(\eta) \ell_k(\zeta),
\tag{2.27}
$$

$$
\mathbf{w}(\mathbf{x}(\xi, \eta, \zeta)) = \sum_{l=1}^{3} \hat{\mathbf{x}}_l \sum_{p,q,r=0}^{n_p, n_q, n_r} \omega_l^{pqr} \ell_p(\xi) \ell_q(\eta) \ell_r(\zeta).
\tag{2.28}
$$

Substituting Equations (2.28) and (2.27) into (2.18) using quadrature equation, Equation (2.26), we obtain the elemental mass and stiffness matrices on the local domain. We need to assemble the local matrices into a global matrix in which we

22

have to sum the contribution of local elements on the common points (points which are at the boundaries and are common between elements). Therefore for the global system we have,

$$\mathbf{M}\ddot{\mathbf{U}} + \mathbf{K}\mathbf{U} = \mathbf{F}, \tag{2.29}$$

where $\mathbf{U}$ is the displacement vector of the global system containing the displacement at all the grid points in the global mesh. $\mathbf{M}$, $\mathbf{K}$ and $\mathbf{F}$ are the global diagonal mass, the global stiffness and the global force matrices. Using GLL points leads to a diagonal mass matrix and therefore simplifies the scheme. Finally, we use the FDM in Equation (2.29) for the time derivative. In these methods, one should consider two factors: the number of grid points per wavelength (i.e., numerical dispersion condition) and the Courant-Friedrichs-Lewy (CFL) stability condition. The first one is a measure of how well the mesh samples the wavefield and the second one ensures that you have a stable simulation by giving a maximum time step for the explicit time integration scheme. Both of these factors reflect the quality of the mesh and are related to the grid spacing and velocity of the medium and time step of the simulation (e.g., Komatitsch and Tromp, 2002; Martin et al., 2008).

The numerical modelling technique (i.e., the SEM) that we described above will be used to model the wavefield in a cracked medium. From this, we can extract quantities such as stresses, strains and displacements on each mesh point within the medium, which we need for our calculations. We then need to introduce an effective medium theory to simplify a cracked medium or, in other words, to estimate the average effect of cracks in the medium rather than having to sum the individual contribution of each crack.

2.3 Effective Medium Theory

Effective medium theories tell us how to average small-scale structures (e.g., cracks) in order to get an effective stiffness tensor, which is used to calculate effective P- and S-wave velocities. In this study, we use the effective medium theory presented by Schoenberg and Sayers (1995) in which the fractures are modelled in a rock using a total compliance tensor, s_{ijkl} (i.e., the inverse of stiffness tensor, c_{ijkl}), as the sum of background and fracture compliance tensors. For a cracked solid,

$$\langle \varepsilon_{ij} \rangle = s^b_{ijkl} \langle \sigma_{kl} \rangle + \frac{1}{2V} \sum_q \int_{S_q} ([u_i]n_j + [u_j]n_i) dS, \tag{2.30}$$

where s^b_{ijkl} is the compliance tensor of the unfractured background, S_q is the surface of the qth fracture in the volume, V, n_i are the unit normals to the fracture and $[u_i]$ are the crack opening and closing displacements known as displacement discontinuities. The symbol $\langle \cdot \rangle$ denotes the average over volume.

Considering planar and parallel fractures in a medium, we apply the following assumption, known as linear slip theory (Schoenberg, 1980) in which the displacement discontinuity is linearly related to the average stress tensor,

$$\frac{1}{V} \sum_q \int_{S_q} [u_i] dS \equiv Z_{ij} \langle \sigma_{jk} \rangle n_k, \tag{2.31}$$

where Z_{ij} are the fracture compliance components which are by definition positive values. If we consider the strain resulting from the fractures to be $s^f_{ijkl} \langle \sigma_{kl} \rangle$, we

obtain the following equation by substitution of Equation (2.31) into Equation (2.30),

$$
\begin{aligned}
s^{f}_{ijkl}\langle\sigma_{kl}\rangle &= \frac{1}{2}(Z_{ir}\langle\sigma_{rs}\rangle n_{s}n_{j} + Z_{jr}\langle\sigma_{rs}\rangle n_{s}n_{i}) \\
&= \frac{1}{2}(Z_{ir}n_{s}n_{j} + Z_{jr}n_{s}n_{i})\frac{\delta_{rk}\delta_{sl} + \delta_{rl}\delta_{sk}}{2}\langle\sigma_{kl}\rangle \\
&= \frac{1}{4}(Z_{ik}n_{l}n_{j} + Z_{jk}n_{l}n_{i} + Z_{il}n_{k}n_{j} + Z_{jl}n_{k}n_{i})\langle\sigma_{kl}\rangle
\end{aligned} \qquad (2.32)
$$

Considering fractures that are invariant with respect to a rotation about an axis normal to the fracture (TI system as described in Section 2.1) we use the following equation to reduce the compliance tensor components to only two: Z_N and Z_T the normal and the tangential compliance (e.g., Schoenberg and Sayers, 1995),

$$
Z_{ij} = Z_{N}n_{i}n_{j} + Z_{T}(\delta_{ij} - n_{i}n_{j}). \qquad (2.33)
$$

By substituting Equation (2.33) into Equation (2.32) for the fracture compliance tensor we have,

$$
s^{f}_{ijkl} = \frac{Z_T}{4}(\delta_{ik}n_{l}n_{j} + \delta_{jk}n_{l}n_{i} + \delta_{il}n_{k}n_{j} + \delta_{jl}n_{k}n_{i}) + (Z_N - Z_T)n_{i}n_{j}n_{k}n_{l}. \qquad (2.34)
$$

For example, consider a VTI medium in which the fractures are parallel to the xy plane with the symmetry axis parallel to the z axis (i.e., $\mathbf{n} = [0,0,1]$), Equation (2.34) can be written in following matrix form using Equation (2.4) for the excess (or crack) compliance tensor (see, e.g., Schoenberg and Sayers, 1995),

$$s^f_{ijkl} = \begin{bmatrix} 0 & 0 & 0 & 0 & 0 & 0 \\ 0 & 0 & 0 & 0 & 0 & 0 \\ 0 & 0 & Z_N & 0 & 0 & 0 \\ 0 & 0 & 0 & Z_T & 0 & 0 \\ 0 & 0 & 0 & 0 & Z_T & 0 \\ 0 & 0 & 0 & 0 & 0 & 0 \end{bmatrix}. \tag{2.35}$$

Finally for the compliance tensor in a cracked medium we have,

$$s_{ijkl} = s^b_{ijkl} + s^f_{ijkl}, \tag{2.36}$$

from which we obtain the stiffness tensor by taking the inverse of the compliance tensor,

$$C = S^{-1}. \tag{2.37}$$

In the following section, we reformulate this section in 2D in which we model the problem in the remainder of the thesis.

2.4   2D stress and strain relationship

In this study, we do our simulations in two dimensions. Therefore we simplify the three-dimensional problem to our 2D problem, which is based on plane strain condi-

tions. As mentioned before in an isotropic medium, we have the following relation,

$$
\begin{bmatrix} \sigma_{11} \\ \sigma_{22} \\ \sigma_{33} \\ \sigma_{23} \\ \sigma_{13} \\ \sigma_{12} \end{bmatrix} = \begin{bmatrix} c_{11} & c_{12} & c_{13} & 0 & 0 & 0 \\ c_{21} & c_{22} & c_{23} & 0 & 0 & 0 \\ c_{31} & c_{32} & c_{33} & 0 & 0 & 0 \\ 0 & 0 & 0 & c_{44} & 0 & 0 \\ 0 & 0 & 0 & 0 & c_{55} & 0 \\ 0 & 0 & 0 & 0 & 0 & c_{66} \end{bmatrix} \begin{bmatrix} \varepsilon_{11} \\ \varepsilon_{22} \\ \varepsilon_{33} \\ \varepsilon_{23} \\ \varepsilon_{13} \\ \varepsilon_{12} \end{bmatrix}. \tag{2.38}
$$

In plane strain, the length of the third dimension is much larger than the other two dimensions. The strains associated with the third dimension (here, assuming our third dimension is the dimension related to the cartesian coordinate of 3) are set to zero,

$$
\varepsilon_{33} = \varepsilon_{13} = \varepsilon_{23} = 0. \tag{2.39}
$$

Substituting Equation (2.39) into Equation (2.38) yields,

$$
\begin{bmatrix} \sigma_{11} \\ \sigma_{22} \\ \sigma_{12} \end{bmatrix} = \begin{bmatrix} c_{11} & c_{12} & 0 \\ c_{21} & c_{22} & 0 \\ 0 & 0 & c_{66} \end{bmatrix} \begin{bmatrix} \varepsilon_{11} \\ \varepsilon_{22} \\ \varepsilon_{12} \end{bmatrix}, \tag{2.40}
$$

and,

$$
\sigma_{33} = c_{31}\varepsilon_{11} + c_{32}\varepsilon_{22}. \tag{2.41}
$$

We get the inverse of Equation (2.40) to get the compliance matrix as follows,

$$
\begin{bmatrix} \varepsilon_{11} \\ \varepsilon_{22} \\ \varepsilon_{12} \end{bmatrix} = \begin{bmatrix} s_{11} & s_{12} & 0 \\ s_{21} & s_{22} & 0 \\ 0 & 0 & s_{66} \end{bmatrix} \begin{bmatrix} \sigma_{11} \\ \sigma_{22} \\ \sigma_{12} \end{bmatrix}. \tag{2.42}
$$

27

Equation (2.42) is the stress and strain relation in terms of the compliance matrix for a 2D plane strain formulation. In order to get the effective compliance matrix in a cracked material, we sum the background compliance components with the crack compliance component using Equation (2.34). For example for a VTI medium, the total or effective compliance matrix is,

$$
S = \begin{bmatrix} s_{11}^t & s_{12}^t & 0 \\ s_{21}^t & s_{22}^t & 0 \\ 0 & 0 & s_{33}^t \end{bmatrix} = \begin{bmatrix} s_{11}^b & s_{12}^b & 0 \\ s_{21}^b & s_{22}^b + Z_N & 0 \\ 0 & 0 & s_{66}^b + Z_T \end{bmatrix},
\tag{2.43}
$$

from which we can get the total or effective stiffness matrix C by Equation (2.37). Then we can get the effective P-wave speed of the medium,

$$
V_p^{eff} = \sqrt{\frac{c_{22}^t}{\rho}}.
\tag{2.44}
$$

This equation is derived from the stiffness matrix where the associated component (here c_{22}^t) is related to the P-wave velocity of the medium along the 2-direction.

Now that we have introduced the crack compliances and displacement discontinuity, we discuss them in more detail in the following section.

2.5 Crack compliance tensor calculations

In the linear slip theory on a fracture boundary, the traction is continuous, but the displacement is allowed to be discontinuous. In this case, the displacement discontinuity is linearly related to the traction by a fracture compliance matrix, Z (e.g.,

Coates and Schoenberg, 1995; Kachanov, 1992),

$$\Delta\mathbf{u} = Z\boldsymbol{\sigma} \cdot \mathbf{n}, \qquad (2.45)$$

or in a component form,

$$\Delta u_i = Z_{ij}\sigma_{jk}n_k, \qquad (2.46)$$

where $\Delta\mathbf{u}$ is the displacement discontinuity (not the Laplacian), and $\boldsymbol{\sigma} \cdot \mathbf{n}$ is the traction acting across the fracture with $\mathbf{n}$ being the unit normal to the fracture as shown in Figure 2.1 for our case defining as $\mathbf{n} = (0, 1)$.
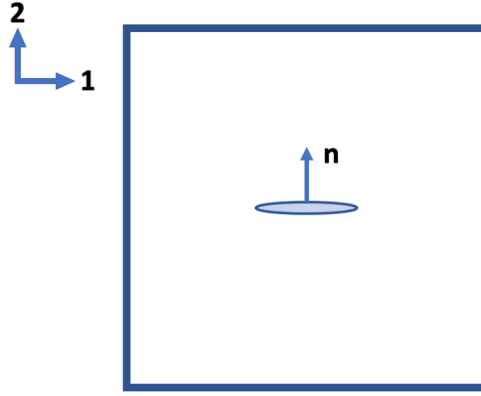

Figure 2.1: $\mathbf{n}$ is the unit normal to the crack's surface. 1 and 2 are defined for the cartesian coordinates.

In our 2D case, we have two displacement discontinuities in directions 1 and 2 (1 and 2 are defined in Figure 2.1). Therefore we can write,

$$\Delta u_1 = Z_{1j}\sigma_{jk}n_k,$$
$$\Delta u_2 = Z_{2j}\sigma_{jk}n_k. \qquad (2.47)$$

By expanding we can write,

$$\Delta u_1 = Z_{11}\sigma_{1k}n_k + Z_{12}\sigma_{2k}n_k + Z_{13}\sigma_{3k}n_k,$$
$$\Delta u_2 = Z_{21}\sigma_{1k}n_{12} + Z_{22}\sigma_{2k}n_k + Z_{23}\sigma_{3k}n_k. \tag{2.48}$$

Assuming rotationally invariant fracture sets, we can simplify the fracture compliance matrix using Equation (2.33), from which we get,

$$\text{if}: i \neq j \quad \Rightarrow \quad Z_{ij} = 0. \tag{2.49}$$

Therefore the fracture compliance matrix has only two components: normal and tangential (i.e., ii; 11 and 22). This leads the fracture behaviour to be invariant with respect to rotation about an axis normal to the fracture. Having this, Equation (2.48) can be written as,

$$\Delta u_1 = Z_{11}\sigma_{11}n_1 + Z_{11}\sigma_{12}n_2,$$
$$\Delta u_2 = Z_{22}\sigma_{21}n_1 + Z_{22}\sigma_{22}n_2. \tag{2.50}$$

Substituting Equation (2.33) into Equation (2.50) and setting n to be the outward unit normal ($\mathbf{n} = [0, 1]$) we get,

$$\Delta u_1 = Z_T\sigma_{12},$$
$$\Delta u_2 = Z_N\sigma_{22}, \tag{2.51}$$

from which we can calculate the crack compliance components from the displacement discontinuity and stress components in which one should be careful not to divide by zero. We calculate u_i and σ_{ij} as part of the SEM calculations. Then we calculate the displacement discontinuity on a crack by,

$$\Delta\mathbf{u} = \mathbf{u}_{crack}^{top} - \mathbf{u}_{crack}^{bot}, \tag{2.52}$$

where the subscript *crack* indicates the displacement is taken from the crack boundary. The superscripts *top* and *bot* represent the top boundary and bottom boundary of a crack inside a medium, respectively. From this, $\Delta\mathbf{u}$ is an indication of opening and closing of the crack.

In the general description from Coates and Schoenberg (1995), Equation (2.45) is implemented as a boundary condition across a fault in the modelling code where the crack compliance components are defined in the medium. Therefore the displacement discontinuity is calculated on the boundaries during the wave propagation as is done by Rusmanugroho et al. (2020). However, in this study, we use the above procedure for calculation of the crack compliance components, and hence the displacement discontinuity. We model the crack as a low-velocity zone and do not explicitly incorporate the linear slip theory into the modelling code.

We now have all the necessary information. However, we need to introduce how to average the quantities on a surface as this is used in one of the ways we calculate the effective P-wave velocity.

2.6   Averaging surface

In Section 2.3, we introduced the formulation of linear slip effective medium theory (e.g., Equations (2.30) and (2.31)) in which we need the average stress and strain components to get the effective stiffness tensor from which we calculate the effective P-wave velocity of the medium. In this part, we explain how we average the stress and strain components. First, we need to understand the Trapezoidal rule for integration in order to average since we use this rule to get the average of the components in the medium.

2.6.1 Trapezoidal rule

The trapezoidal rule is generally used to integrate functions, but here we use it to compute an area. This is more complicated with spectral element meshes than with finite-difference meshes because these meshes are not rectilinear. It first divides the area into trapezoids. The area of a trapezoid is the area of the base times its average height. The base of a trapezoid has length Δx and its sides have heights y_{i-1} and y_i. If Δx is small enough, then the trapezoid i has the approximate area of $\Delta x \dfrac{(y_{i-1} + y_i)}{2}$.

When we add the areas of all the trapezoids under the curve, we get,

$$
\begin{aligned}
\text{Area} \; &= \; \Delta x \left\{ \tfrac{y_o + y_1}{2} + \tfrac{y_1 + y_2}{2} + \tfrac{y_2 + y_3}{2} + ... + \tfrac{y_{n-1} + y_n}{2} \right\} \\
&= \; \Delta x \left(\tfrac{y_o}{2} + y_1 + y_2 + ... + y_{n-1} + \tfrac{y_n}{2} \right).
\end{aligned}
\tag{2.53}
$$

2.6.2 Averaging using boundaries of the surface

As mentioned above, we need the average components of stress and strain, and these volume averages can be written as, (e.g., Hashin, 1963; Kachanov, 1992),

$$
\langle \varepsilon_{ij} \rangle = \frac{1}{2V} \int_S (u_i n_j + u_j n_i) dS,
\tag{2.54}
$$

where n_i is the unit normal to the boundary of the surface, and u_i is the displacement which can be written as,

$$
u_i = \varepsilon_{ik} x_k,
\tag{2.55}
$$

and

$$
\langle \sigma_{ij} \rangle = \frac{1}{2V} \int_S (T_i x_j + T_j x_i) dS,
\tag{2.56}
$$

where x_i is the cartesian coordinate of points on the boundary (with the origin at the centre of the averaging volume) and T is the traction defined as,

$$T_i = \sigma_{ik}n_k. \tag{2.57}$$

For a surface average we then have,

$$
\begin{aligned}
\langle \varepsilon_{ij} \rangle &= \frac{1}{2S} \int_l (u_i n_j + u_j n_i) dl, \\
\langle \sigma_{ij} \rangle &= \frac{1}{2S} \int_l (T_i x_j + T_j x_i) dl.
\end{aligned}
\tag{2.58}
$$

To compute the average stress and strain, we first plug Equations (2.55) and (2.57) into (2.58). Then considering Figure 2.2 that shows our surface of interest with 4 boundaries, we expand the equation into each element and for each boundary with n_i being a component of outward normal. This gives (details of the steps are shown in Appendix A.1):
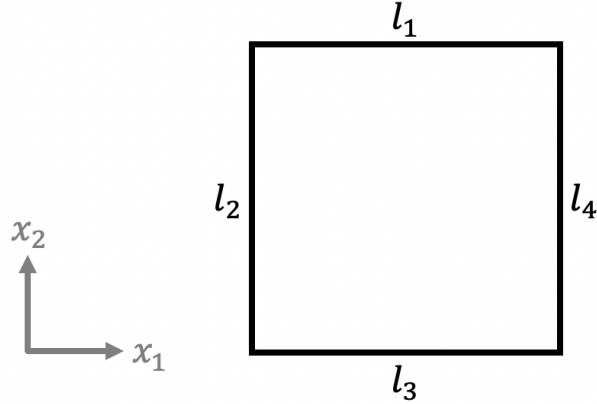

Figure 2.2: Averaging surface with 4 boundaries.

$$
\begin{aligned}
\langle \varepsilon_{11} \rangle &= \frac{1}{S}\left[\int_{l_2} -(\varepsilon_{11}x_1 + \varepsilon_{12}x_2)dl_2 + \int_{l_4}(\varepsilon_{11}x_1 + \varepsilon_{12}x_2)dl_4 \right], \\
\langle \varepsilon_{22} \rangle &= \frac{1}{S}\left[\int_{l_1}(\varepsilon_{22}x_2 + \varepsilon_{21}x_1)dl_1 - \int_{l_3}(\varepsilon_{22}x_2 - \varepsilon_{21}x_1)dl_3 \right], \\
\langle \varepsilon_{12} \rangle &= \frac{1}{2S}\left[\int_l(\varepsilon_{11}x_1 + \varepsilon_{12}x_2)dl_1 - \int_{l_2}(\varepsilon_{21}x_1 + \varepsilon_{22}x_2)dl_2 - \right. \\
&\qquad \left. \int_{l_3}(\varepsilon_{11}x_1 + \varepsilon_{12}x_2)dl_3 + \int_{l_4}(\varepsilon_{21}x_1 + \varepsilon_{22}x_2)dl_4 \right],
\end{aligned}
\tag{2.59}
$$

$$
\begin{aligned}
\langle \sigma_{11} \rangle &= \frac{1}{S}\left[\int_l \sigma_{12}x_1 dl_1 - \int_{l_2}\sigma_{11}x_1 dl_2 - \int_{l_3}\sigma_{12}x_1 dl_3 + \int_{l_4}\sigma_{11}x_1 dl_4 \right], \\
\langle \sigma_{22} \rangle &= \frac{1}{S}\left[\int_{l_1}\sigma_{22}x_2 dl_1 - \int_{l_2}\sigma_{21}x_2 dl_2 - \int_{l_3}\sigma_{22}x_2 dl_3 + \int_{l_4}\sigma_{21}x_2 dl_4 \right], \\
\langle \sigma_{12} \rangle &= \frac{1}{2S}\left[\int_l(\sigma_{12}x_2 + \sigma_{22}x_1)dl_1 - \int_{l_2}(\sigma_{11}x_2 + \sigma_{21}x_1)dl_2 - \right. \\
&\qquad \left. \int_{l_3}(\sigma_{12}x_2 + \sigma_{22}x_1)dl_3 + \int_{l_4}(\sigma_{11}x_2 + \sigma_{21}x_1)dl_4 \right].
\end{aligned}
\tag{2.60}
$$

Equations (2.59) and (2.60) are used to calculate the average strains and stresses on a surface of interest, respectively. Applying the Trapezoidal rule on each integral (i.e., for each boundary) and doing summation of all four boundaries gives the average value for each element of the stress or strain on the surface of interest.

So far, we have introduced all the necessary theories. In this study, we have implemented all the theories discussed except for the implementation of the spectral element method for which we use an open-source code. More details are provided in the next chapter.

Chapter 3

Estimating travel-time perturbations

Having set up all of the necessary theories in the last chapter, we now implement these theories and discuss some of the implementation details as well as some results in this chapter. Since the goal of this study is to better understand fractured media by studying P-wave travel-time delay perturbations, we show the whole procedure of P-wave travel-time delay calculations. First, we explain the wavefield modelling procedure. Next, we provide three ways to calculate the effective P-wave velocity of the medium and then we choose one and justify our choice. After that, we show how to calculate the P-wave travel-time delay caused by the pump perturbation. The following steps provide a general procedure with the output of each step being the input of the following step:

1) Model the pump wavefield, which gives the stress and displacement components on the mesh points.

2) Calculate the effective P-wave velocity.

3) Calculate the P-wave travel-time delay.

These steps are discussed in more detail in the following sections.

3.1   Wavefield simulations

The first step is to model the wavefield through the rock. As mentioned earlier, we choose SEM as our numerical method for wave propagation simulations. We use the open-source code SPECFEM2D (available at: `https://geodynamics.org/cig/software/specfem2d/`) to do our simulations (e.g., Komatitsch and Vilotte, 1998). The source code is able to use unstructured meshes generated by an external software like Trelis (CUBIT) (available at: `https://www.csimsoft.com/trelis`) (e.g., Martin et al., 2008) which is the software we use in our study. The first step in our simulations is to generate an unstructured mesh. After that, we use the open-source code MeshAssist (available at: `https://github.com/homnath/MeshAssist.git`) developed by Gharti et al. (2017) to convert the output format of Trelis to the input format of SPECFEM2D. We need to check the quality of the mesh, which is done using the build function in the SPECFEM2D package. Skewness (i.e., deformation of the element angles) of the whole mesh gives one measure of mesh quality and should be less or equal to about 0.75 based on the information provided in the package (see also Martin et al., 2008). We repeat the meshing process until we get a good quality mesh. Another criterion that we should consider is to check that the mesh will appropriately sample the wavefield based on the medium and source parameters. This is also a part of the functionality of the build function in the package. Therefore, after we make the mesh and set input the simulation parameters shown in Table 3.1 as well as the source frequency, the code allows us to check how the mesh samples the wavefield based on a default threshold. The defined threshold value is around

4.5 points per S-wavelength in elastic regions and 5.5 per P-wavelength so that the frequency content of the wave is accurately preserved. After this, we need to choose a time step for our calculations to satisfy the CFL condition (CFL value below 0.5).

Table 3.1: Modelling Parameters

	Host rock	Crack
$V_p(m/s)$	2954	2806.3
$V_s(m/s)$	1829	1691.8
$\rho(kg/m^3)$	2285	2227.9

As shown in Figure 3.1, our 2D model is 15 cm $\times$ 15 cm. An elliptical horizontal crack with a major radius of 0.5 cm and a minor radius of 75 μm is embedded at the centre of the model. The model has 149473 elements. We use 143 three-cycle sine wave sources at the left of the model to act as a plane wave. The frequency of our sources is 50 kHz, and the time step for our calculations is 0.4 ns. The values of the physical properties of the model are given in Table 3.1. These parameters are chosen to be similar to the parameters used by Rusmanugroho et al. (2020).
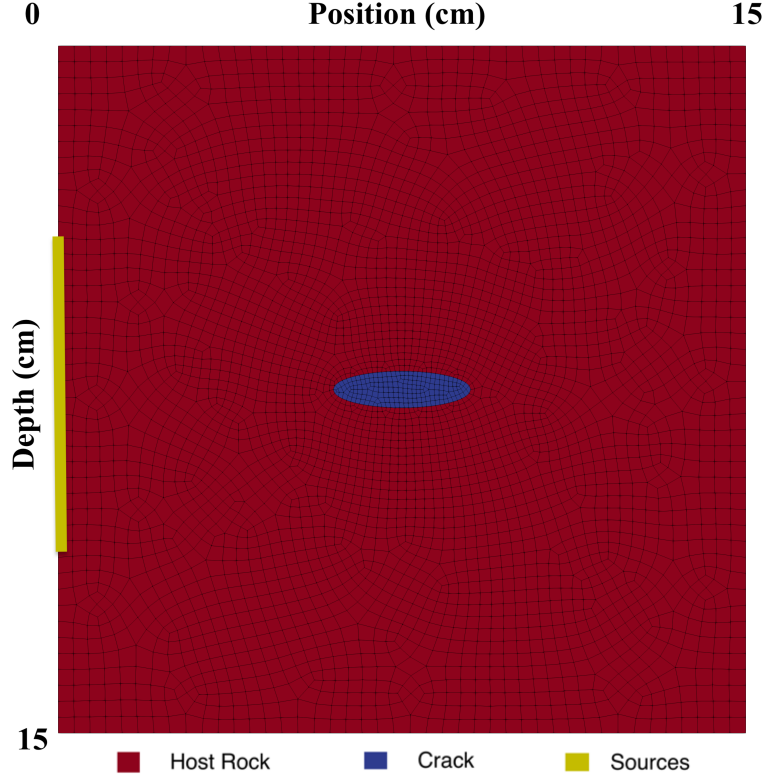
Figure 3.1: Our rock model with unstructured mesh. The crack and the meshing size are exaggerated for visualization purpose. The picture is plotted using ParaView software (available at: `https://www.paraview.org`).

Figure 3.2 shows a wavefield snapshot of the z component of the stress. We present the wavefield to show that our sources first propagate P-waves and then S-waves and are not pure S-wave sources. In TenCate et al. (2016) and Rusmanugroho et al. (2020), the S-wave source (pump) perturbs the medium, and the P-wave source (probe) senses the perturbation by its passage through the medium in a perpendicular direction to the pump direction. Despite those studies, we do not send a probe to sense the perturbation explicitly. However, we use the effective P-wave velocity to send an "imaginary" probe through the medium. Note that the sources are shifted down to make sure the embedded crack, which is at the centre of the rock, is not aligned with the place that the S-wave produces a near-zero amplitude.
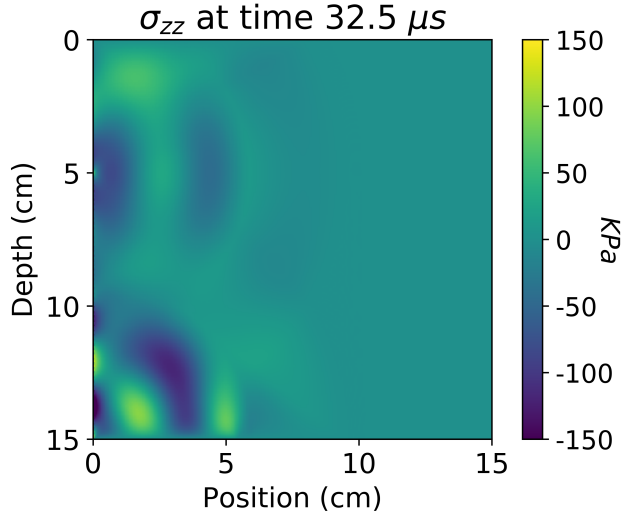
Figure 3.2: A wavefield snapshot of the z component of the stress.

Now that we have set up all of the necessary parameters, we can run the simulations. The simulations give us the strains and the stresses on each element as well as the displacements on the provided receivers' positions. These quantities are all that we need for our purpose. Therefore we can continue to calculate the effective P-wave velocity. Before discussing that calculation, we mention a few major differences between our study and a similar study done by Rusmanugroho et al. (2020).

Rusmanugroho et al. (2020) do the simulations in 3D using FDM, where they implement the linear slip theory into the modelling code. By contrast, here we do the simulations in 2D using SEM and use the linear slip theory after the wavefield modelling when we calculate the effective P-wave velocity. Also, they implement the nonlinear wave equation, while the linear wave equation is implemented in the SEM open-source code. We implement and compare a few different ways of calculating the effective P-wave velocity, as well as the P-wave travel-time delay calculation method. Note that the procedure for the P-wave velocity calculations is slightly different from Rusmanugroho et al. (2020)'s study. The main difference is that we calculate the displacement discontinuity by the subtraction of the bottom boundary from the top

boundary of the crack, whereas they use the displacement discontinuity coming from the implementation of linear slip into the FDM code. The travel-time calculations are similar in both studies, but the difference is that we calculate the travel-time of the P-wave probe directly from the velocity field using a simple ray-tracing method while they propagate the P-wave probe into the medium. More details of our methods and implementations are provided in the following sections.

3.2   Effective P-wave velocity calculations

In this section, we compare three methods of effective P-wave velocity calculation in a medium. We expect that the effective P-wave velocity perturbation of the medium to be small and negative (see, e.g., Rusmanugroho et al., 2020). It should be small because the crack is small compared to the background, and it should be negative because, in the definition, we have positive crack compliances (see, Section 2.3), which results in negative velocity perturbations (i.e., the perturbed velocity is smaller than the background velocity). Based on this, we choose one method to continue for further analysis. To do so, we use the model and simulation parameters provided in the previous section.

3.2.1   Effective P-wave velocity calculations using averaging on a surface

Two of the three methods of effective P-wave velocity calculations use the method of averaging quantities on an arbitrary surface. The first is to use the stress and strain relationship from Hooke's law, and the second is using the displacement discontinuity and hence the crack compliance. In the following sections, we introduce each of these methods in more detail.

3.2.1.1 Stress-strain relationship

Based on Equation (2.43), which comes from the effective medium theory, introducing a horizontal crack in the medium only affects two specific components of the compliance matrix; s_{22}^t and s_{33}^t. Knowing this, we can use the plain strain relation of Hooke's law in 2D, Equation (2.42), to directly get those components. So we have,

$$s_{22}^t = \frac{\overline{\varepsilon_{22}} - (s_{21}^t \, \overline{\sigma_{11}})}{\overline{\sigma_{22}}}, \tag{3.1}$$

and

$$s_{33}^t = \frac{\overline{\varepsilon_{12}}}{\overline{\sigma_{12}}}. \tag{3.2}$$

Using these equations, we can calculate the total compliance matrix because the other components are equal to the background components. The notation $\overline{a}$ indicates regular averaging, which is the summation of a on all points divided by the number of mesh points. We then calculate the effective P-wave velocity using Equation (2.44) after inverting the compliance matrix to get the stiffness matrix. Therefore using these explanations for this method, the steps are as follows:

1) Average the stresses and strains on a surface of interest (regular averaging).

2) Calculate the total (i.e., effective) compliance components using Equations (3.1) and (3.2) and the other components using parameters in Table 3.1.

3) Invert the total compliance matrix to get the total stiffness matrix.

4) Use Equation (2.44) to calculate the effective P-wave velocity.

Plots (a) and (b) in Figure 3.3 show the numerator and denominator ($\sigma_{22} = \sigma_{zz}$) of Equation (3.1) for two different averaging surfaces. The corresponding recovered effective P-wave velocity of the medium (obtained by dividing the numerator (blue)

by the denominator (red)) are shown in plots (c) and (d). The velocity jumps are related to dividing by a near-zero value. The effective P-wave velocity perturbations start at about the time that the first P-wave passes the crack.
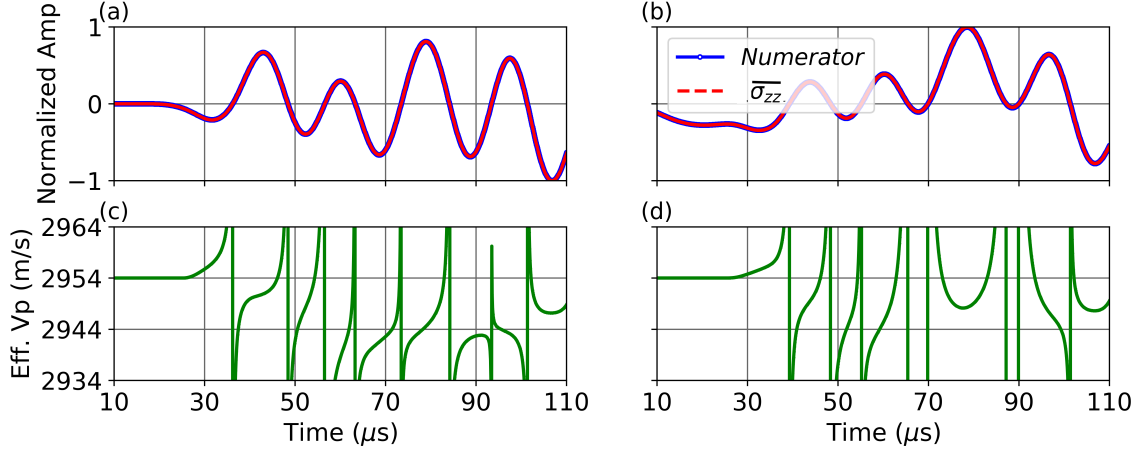

Figure 3.3: (a) and (b) are the normalized average z component of the stress and the numerator of Equation (3.1) for averaging surface of 5 cm × 5 cm and 15 cm × 15 cm respectively. The corresponding effective P-wave velocity plots are shown in (c) and (d) respectively.

This method is easy to implement since we only need the average stress and strain components on the mesh. However, the magnitude of the velocity perturbations in this method is not realistic. We conclude this because we have embedded a small crack in the medium, and the velocity perturbations are large compared to the background value, the values observed in the lab (TenCate et al., 2016) and the values calculated in other ways (Rusmanugroho et al., 2020). If we use the average velocity of the medium based on the surface of the crack and background, we expect an average velocity of about 2953.9 m/s while we have much lower velocities in Figure 3.3.

3.2.1.2 Using the crack compliance matrix

In the previous method, we only use the stress and strain relation, to directly get the average (or total) compliance tensor of the medium. Here, we use the displacement

discontinuities and the stress components to get the excess (or fractured) compliance matrix, and then we add this to the background (i.e., without fractures) compliance matrix to get the total compliance matrix. In this method, first, we use Equation (2.60) and the trapezoidal rule of integration to get the average stress components on a surface of interest using boundaries of that surface (see, Section 2.6). To do so, we interpolate the mesh to have a structured mesh on the boundary. Next, we calculate the displacement discontinuities using Equation (2.52). We compute the displacement discontinuities by subtracting the bottom boundary of the crack from the top boundary. Then using Equation (2.51), we calculate the crack compliance components. After this, we use Equation (2.43) to obtain the total compliance matrix of the medium. Finally, by getting the inverse of the compliance matrix, we get the stiffness matrix from which we can calculate the effective P-wave velocity using Equation (2.44). These steps are summarized as:

1) Interpolate the stress quantities from the unstructured mesh to a structured mesh.

2) Use Equation (2.60) and the trapezoidal rule of integration to get the average stress components.

3) Use the trapezoidal rule of integration to sum the displacement components on the crack boundaries and then calculate the displacement discontinuity using Equation (2.52) and then average it on the surface.

4) Calculate the crack compliance components using Equation (2.51).

5) Use Equation (2.43) to obtain the total compliance matrix of the medium.

6) Invert the total compliance matrix to get the total stiffness matrix.

7) Use Equation (2.44) to calculate the effective P-wave velocity.

43

Note that items 4) and 5) are only valid for horizontal cracks (n=[0,1]). Slight modifications are needed for cracks in other orientations.
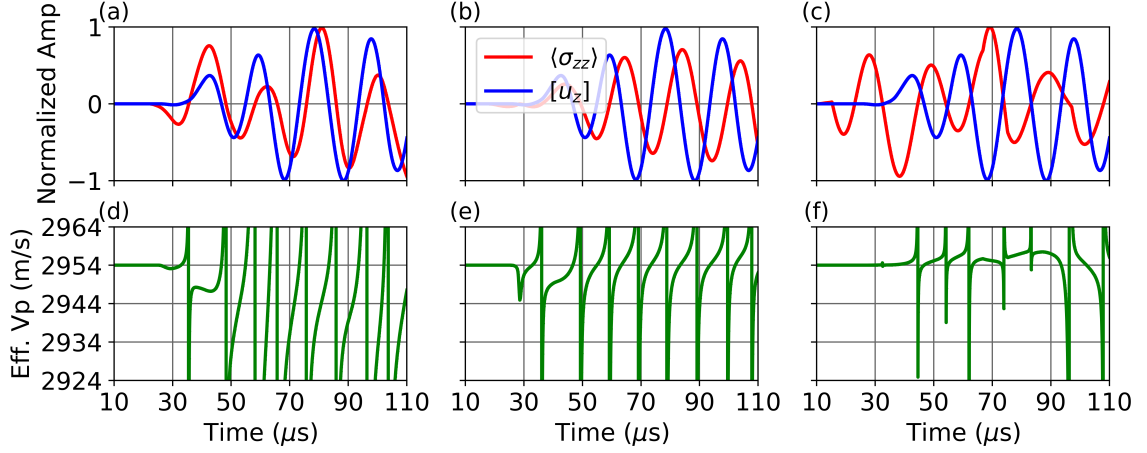

Figure 3.4: (a), (b) and (c) are the normalized average z component of the stress and the z component of the displacement discontinuity for averaging surfaces of $4\lambda \times 4\lambda$, $8\lambda \times 8\lambda$ and $16\lambda \times 16\lambda$ respectively. The $\lambda = 5.908$ mm is the wavelength a P-wave with frequency of 500 kHz. The corresponding effective P-wave velocity plots are shown in (d), (e) and (f) respectively.

As mentioned before, the components of the crack compliance matrix, Z, are positive. We can easily conclude that in Equation (2.51), the stress and displacement discontinuity should have the same sign to satisfy this condition. By looking at the plots (a), (b) and (c) in Figure 3.4 that represent plots for three different averaging surfaces, we see that the displacement discontinuity and the stress components are not in phase which leads to negative crack compliances (see Figure 3.5) which is not correct. This is why we get the positive velocity perturbations seen in plots (d), (e), and (f), which correspond to plots (a), (b), and (c), respectively. These plots show that the calculations depend strongly on the choice of averaging surface. As with the previous method, the velocity jumps are related to dividing by a near-zero number. Note that the discontinuities in the average stress (red line) in the plot (c) at times about 67 μs and 97 μs are related to when the wave reaches the right boundary of

44

the averaging surface for the first time and the second time when it is reflected back from the free surface boundary respectively.
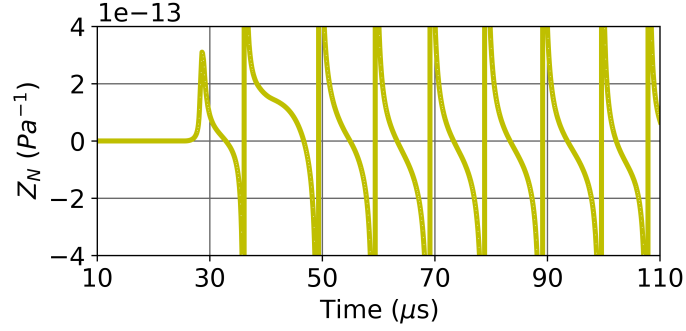

Figure 3.5: Crack normal compliance, Z_N. This plot corresponds to plots (b) and (e) in Figure 3.4.

As an example, Figure 3.5 shows the crack normal compliance plot which corresponds to plots (b) and (e) in Figure 3.4. The shape of the oscillations of Z_N is similar to a cotangent function, which is a cosine function over a sine function. This comes from dividing the displacement discontinuity by the stress, both of which are like sine or cosine functions. The other feature is that the effective V_P plot (Figure 3.4 (e)) is the inverse of this normal crack compliance (tangent function). This is because we take the inverse of the compliance matrix to get the stiffness matrix and then use the same component related to the P-wave velocity polarized along the z direction when we calculate the effective V_P. In summary, this method results in un-physical negative crack compliances or positive velocity perturbations, which are not observed experimentally nor expected since the crack has a lower velocity than the surrounding material. This suggests that we need to have another method to solve the problem, which we are going to explain in the following section.

45

3.2.2 Effective P-wave velocity calculations using quantities on the crack boundaries

In the previous method, we had the problem of getting negative crack compliance. To solve the problem, we go back to the linear slip theory, where the displacement discontinuity is linearly related to the stress on the boundary of two elastic media (see, Section 2.5). In the previous section, Section 3.2.1.2, we used the average of the stress on a surface, while here, in the third method, we use the stress on the crack boundaries (boundaries between two elastic media). The other procedures are exactly as with the second method.

The reason behind this is that assuming a static perturbation (equivalent to a dynamic perturbation with a very low frequency), which the linear slip effective medium theory is based on, results in the stress being the same at different points in the medium. Because we use a dynamic perturbation, there will be a time or phase shift between the displacement discontinuity and applied stress, which causes the negative crack compliances we saw in the previous section. Assuming low-frequency sources (large wavelength with respect to the crack aperture), we use the average stress on the crack boundaries. Therefore the variations in stress and strain are slow enough that we can assume we are in the static case at each time instant and then use the static theory for our dynamic perturbations (see also Rusmanugroho et al., 2020). Therefore, because the relationship between the stress and displacement discontinuity is defined on the boundary of two elastic media, it makes sense to apply the method on the boundary of the crack, rather than on a fictitious boundary as done in the previous method. The steps are as follows:

1) Use the trapezoidal rule of integration to sum the stress components on the top crack boundary. We use the top boundary because we assume the stress is almost

the same as the bottom boundary due to the long wavelength source perturbations.

2) Use the trapezoidal rule of integration to sum the displacement components on the crack boundaries and then calculate the displacement discontinuity using Equation (2.52)

3) Calculate the crack compliance components using Equation (2.51).

4) Use Equation (2.43) to obtain the total compliance matrix of the medium.

5) Invert the total compliance matrix to get the total stiffness matrix.

6) Use Equation (2.44) to calculate the effective P-wave velocity.

The steps are the same as the previous method except for the first two steps, where we have replaced our arbitrary boundary used previously with the boundary of the crack.
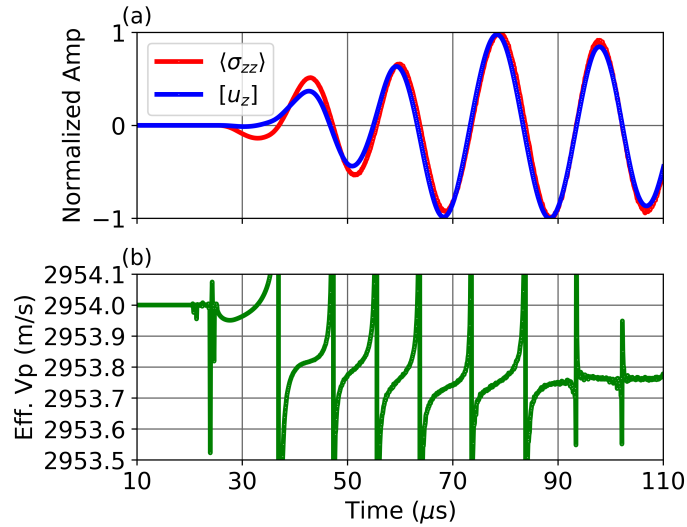

Figure 3.6: The normalized average z component of the stress and the z component of the displacement discontinuity are shown in plot (a). The effective P-wave velocity is shown in (b).

Figure 3.6 shows that the problem of getting negative crack compliances (equivalent to getting positive velocity perturbations) is solved with this method. After

47

using this method, the problem of shifting curves of displacement discontinuity and stress with respect to each other is solved, and now they almost fall on each other in plot (a). Similar to before, the velocity jumps in plot (b) are related to the division over a near-zero value. Also, the velocity perturbations are in agreement with other results now, as we expected based on the surface average velocity of the medium (i.e., the average velocity of about 2953.9 m/s). From these plots, we see that the effective P-wave velocity oscillations are twice in one period of the source wave or in other words, the frequency of the effective P-wave oscillations is twice the frequency of the source.

Since we get reasonable results from this method, we choose this method for further analysis. In the next section, we explain how to calculate the travel-time delay of the medium as this is the other necessary calculation to obtain our results.

3.2.3 Travel-time delay calculations

After calculating the effective P-wave velocity, we calculate the travel-time delay in our model to see how changing the effective P-wave velocities affects the P-wave travel-time through the medium. We calculate the effective P-wave velocity using the method explained in the previous section. Using these velocities as a function of time, we can calculate the travel time of a P-wave along the ray shown in blue in Figure 3.7. The P-wave travels through the medium with the velocity of the medium at a particular time step and moves forward until we get to the other side of the medium (P-wave passes through the whole medium). By summing up the travel-time from each time step, we get the total travel-time. Therefore in each time step the P-wave moves by a distance of $h_i = \delta t_i \times V_{p_i}^{eff}$ where $V_{p_i}^{eff}$ is the velocity associated with that time step, δt_i. We continue until the summation over all of the h_is is equal to 15 cm, which is the size of the rock. Then we sum all the time steps to get the

total travel-time. In the end, we subtract the travel-time of a medium without any perturbations (or no crack) from this value to get the travel-time delay caused by the sources' perturbation in the medium. This procedure is repeated again by shifting the time that we initiate the propagation of the "imaginary" P-wave probe to mimic the experimental results.
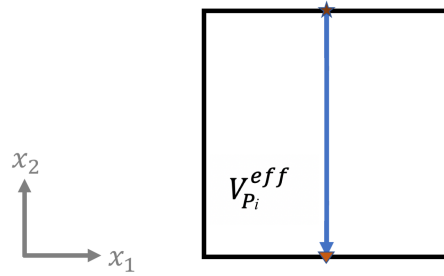

Figure 3.7: We calculate travel-time of a straight ray from the star to triangle shown by blue arrow in our model (black rectangle). $V_{p_i}^{eff}$ is the effective P-wave velocity of the medium at time step δt_i.

Now that we have explained all the procedures for our study, in the next chapter we vary the parameters in the medium and calculate the effective P-wave velocity and the travel-time delay of the P-wave to better understand the behaviour of the medium with these parameter changes.

Chapter 4

Results

In this chapter, we provide the results of this study. We change three model parameters: the crack aperture, the crack velocities and the crack angle (vertical/horizontal). We then calculate the effective P-wave velocity and the P-wave travel-time delays, using the methods described in Chapter 3.

4.1   Crack aperture

The first parameter that we change is the crack aperture. We vary the minor axis of the elliptical crack using the values 0.15 mm, 0.3 mm and 0.6 mm. As we see in Figure 4.1, the effective P-wave velocity change is larger with larger crack apertures.
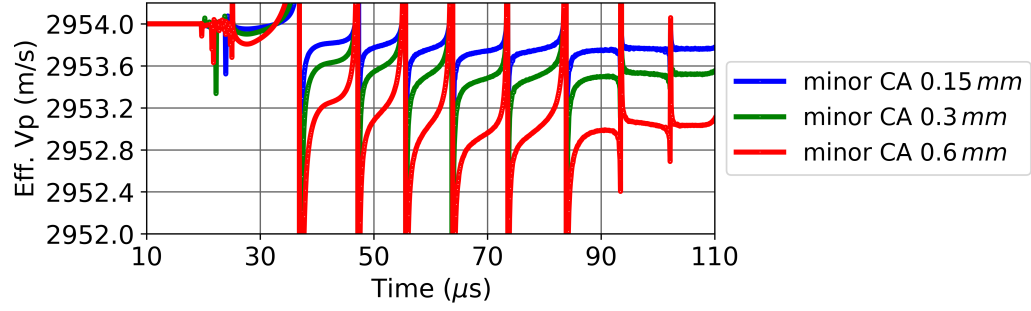
Figure 4.1: Effective P-wave velocity of the medium with crack aperture of 0.15 mm, 0.3 mm and 0.6 mm shown by the blue, green and red lines respectively.

Figure 4.2 shows the corresponding travel-time delay plot for the velocities shown in Figure 4.1. It shows that the larger the crack aperture, the higher the P-wave travel-time delay. In order to produce this plot, we repeat the procedure explained in Section 3.2.3 once for each point on this plot. In other words, we start the pump wave, then wait until the transmission delay (x-axis of Figure 4.2) has elapsed before sending our "imaginary" P-wave. We then use the velocity shown in Figure 4.1 at the appropriate times to compute the travel-time delay for this transmission time. Then we change the transmission time (move to the next point in Figure 4.2) and repeat the procedure.
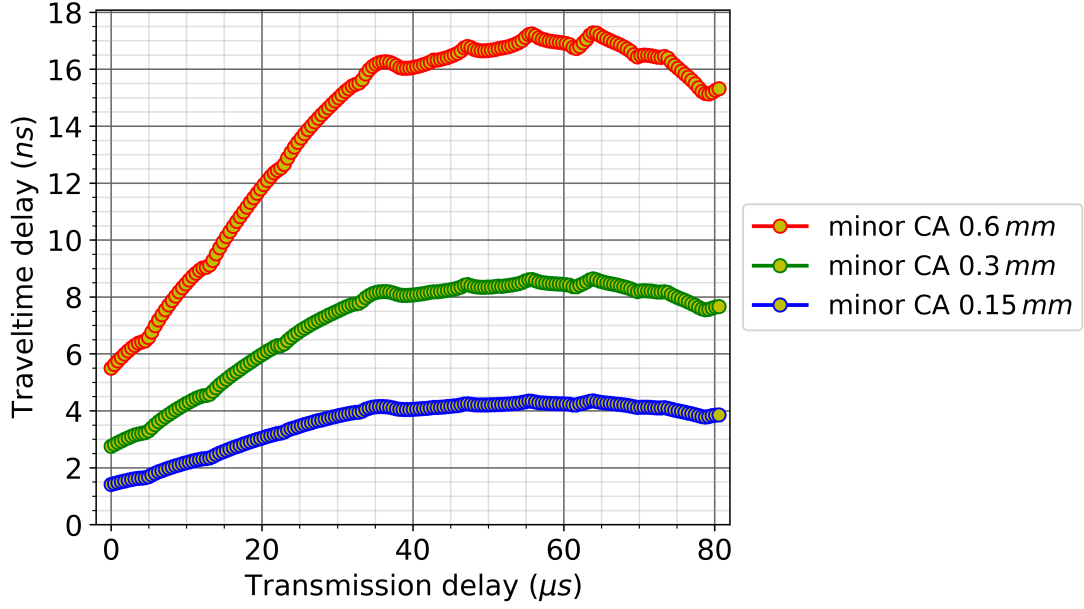
Figure 4.2: P-wave travel-time delay caused by the Pump wave for a crack model with minor radius of 0.15 mm, 0.3 mm and 0.6 mm shown by the blue, green and red lines respectively.

Going into more detail, we see that in the case of a crack aperture of 0.3 mm the delay starts around 2.8 ns and reaches a maximum of 8.6 ns with a difference of 5.8 ns, while in the case of crack aperture of 0.6 mm the delay starts around 5.5 ns and reaches a maximum of 17.3 ns with a difference of 11.8 ns. For the crack aperture of 0.15 mm, the minimum starts from 1.4 ns and reaches a maximum of 4.3 ns with a difference of 2.9 ns. We conclude that the maximum delay is almost proportional to the crack aperture, as shown in Figure 4.3. As stated in Kachanov (1992), the crack compliance tensor depends on a few parameters, including crack size and shape and on elastic properties of the matrix. Since the crack compliance is related to our velocity change and hence the travel-time delay, we provide Figure 4.3 (and later Figure 4.8) to see how changing a crack parameter changes the travel-time delay.
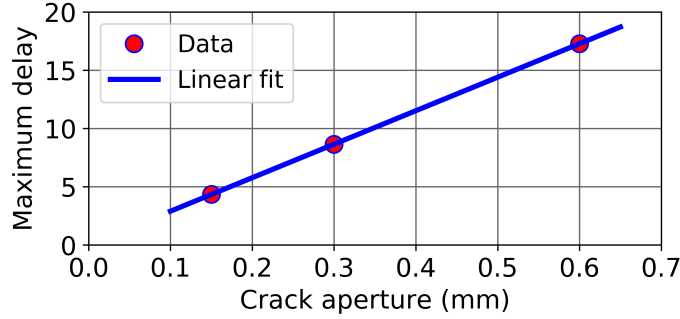
Figure 4.3: A linear fit between the increasing the fracture aperture and the maximum delay.

For better understanding the travel-time delay plots, we show Figure 4.4. The data is from the crack aperture of 0.15 mm in Figure 4.2. By low-pass filtering the data, we see the trend of the data, which is shown by the black curve in the plot. The trend shows that the delay is increasing and reaches its maximum around the time that the S-wave reaches the crack ($\approx$38 μs). To see the frequency content of the data, we choose a few bandpass filters with pass bands that include the frequency of our pump source (50 kHz). In Figure 4.5, we zoom in on the bandpass filtered data. These data show that the data contain oscillations at near, but not exactly the source frequency. This is because of the effective P-wave velocity, which is not oscillating at precisely the source frequency as well as the non-symmetrical shapes of those oscillations (see, Figure 4.1). However, since it is quite close to the source frequency, we explain this results from the pump opening and closing the fracture, and the probe sensing these oscillations hence the travel-time delay follows the trough and peak (opening and closing) of the sine wave sources (see TenCate et al., 2016).
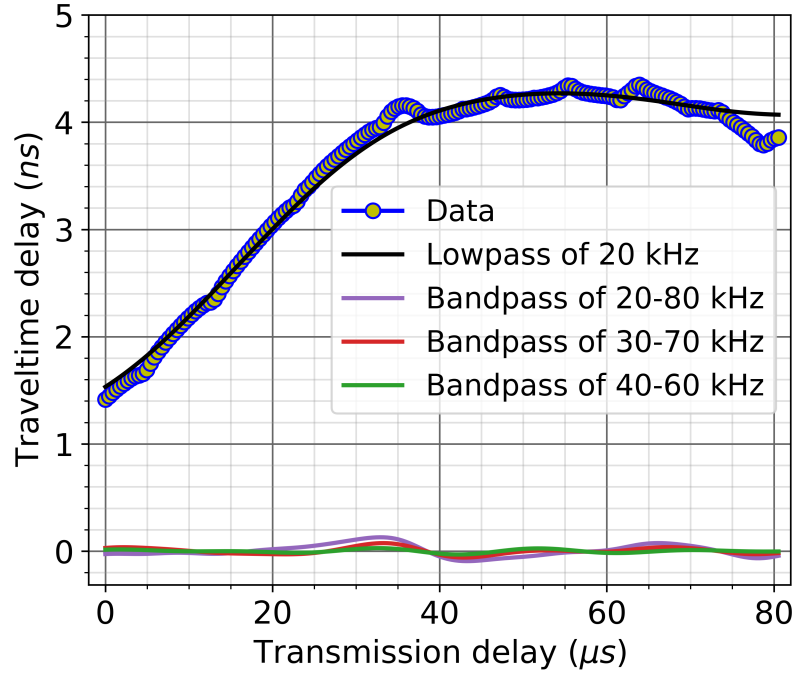
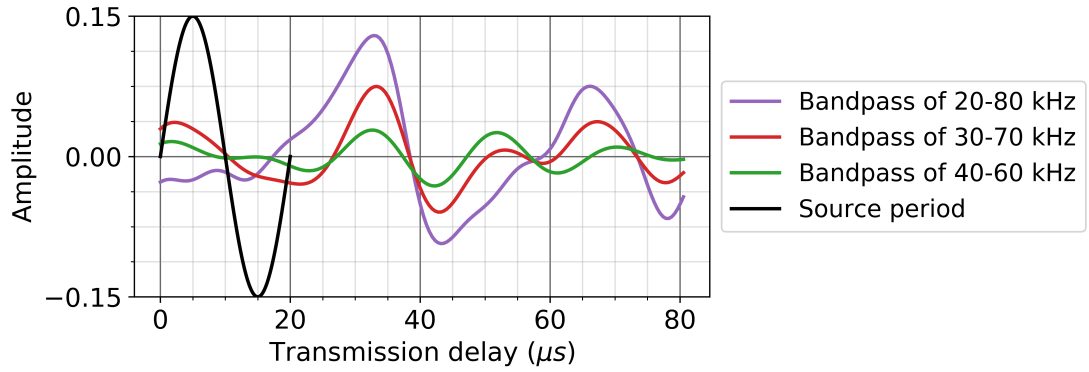Figure 4.4: P-wave travel-time delay for crack aperture of 0.15 mm and the filters applied to the data.

Figure 4.5: Bandpass filters of Figure 4.4 are shown with a closer view.

In the next section, we change the crack velocities using the model with the crack aperture of 0.15 mm.

4.2   Crack velocities and density

In this section, we change the crack velocities relative to the background velocities and compare the effective P-wave velocity and P-wave travel-time delays.

Table 4.1: Crack velocities' parameters as a percentage of the background velocities. The density values do not follow the same rule as the velocities.

		Crack (background %)		
	Background	90%	85%	80%
$V_p(m/s)$	2954	2658.6	2510.9	2363.2
$V_s(m/s)$	1829	1646.1	1554.7	1463.2
$\rho(kg/m^3)$	2285	2170.8	2113.6	2056.5

Figure 4.6 shows the effective P-wave velocity of the medium with three different crack velocities provided in Table 4.1. The results show that as expected, the effective P-wave velocity change is larger, with a larger difference between the background and crack velocities.
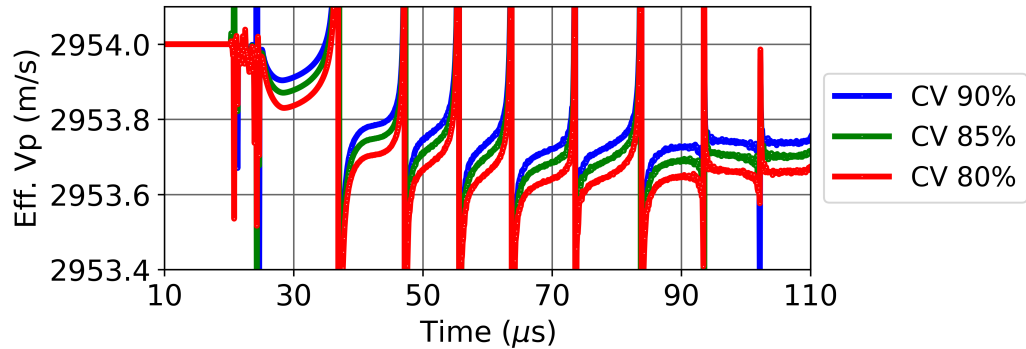

Figure 4.6: Effective P-wave velocity of the medium with crack velocities of 90%, 85% and 80% of the background velocities shown by the blue, green and red lines respectively.

We show the P-wave travel-time delay results in Figure 4.7. The results show that the larger the difference between crack velocities and background velocities, the
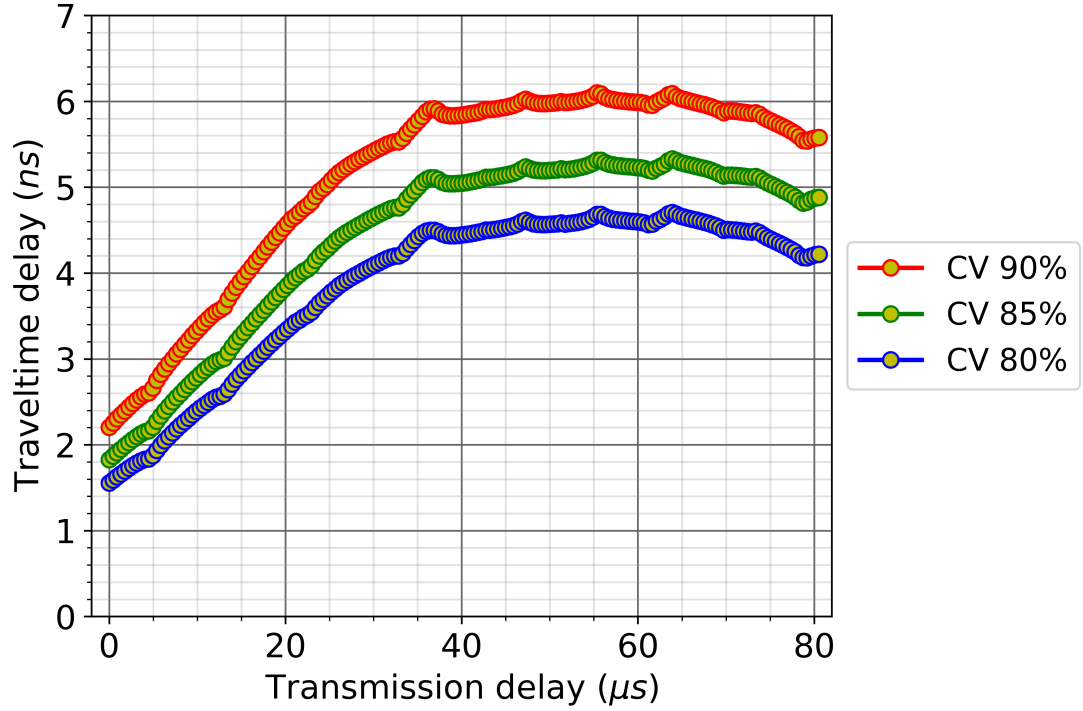
higher the P-wave travel-time delay.

Figure 4.7: P-wave travel-time delay of the medium with crack velocities of 90%, 85% and 80% of the background velocities showing by blue, green and red line respectively.
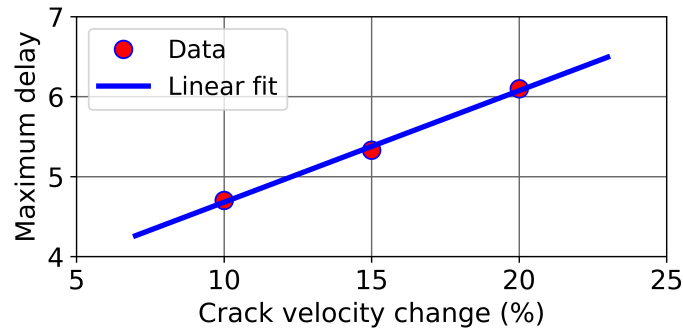

Figure 4.8: A good linear fit between increasing the crack and background velocity difference and the maximum delay.

Figure 4.8 shows that the maximum delay also follows a linear rate with the change of the velocities inside the crack. In the next section, we change the crack orientation to see how this affects the results.

4.3 Vertical crack

Up to this point, all of our experiments have involved a horizontal crack; in this section, we use a vertical crack. Based on Section 2.3, if we use a vertical crack, we have a different unit normal to the fracture, which is now $\mathbf{n} = (1, 0, 0)$. The medium is HTI, as opposed to before, when it was VTI. We have to add the crack normal compliance, Z_N to s_{11}^b instead of s_{22}^b in Equation (2.43), and Equation (2.51) is also different. We use the same model parameters as provided in Table 3.1 and crack aperture of 0.15 mm. Practically within the code, to avoid re-meshing the domain, we simulate this by moving the source from the left-hand side of the model to the top. In this case, Equations (2.43) and (2.51) are the same because the crack normal has not changed. The only change is that we now use c_{11}^t instead of c_{22}^t in Equation (2.44) to calculate the effective P-wave velocity in the direction of perpendicular to the crack normal or along the 1-direction.
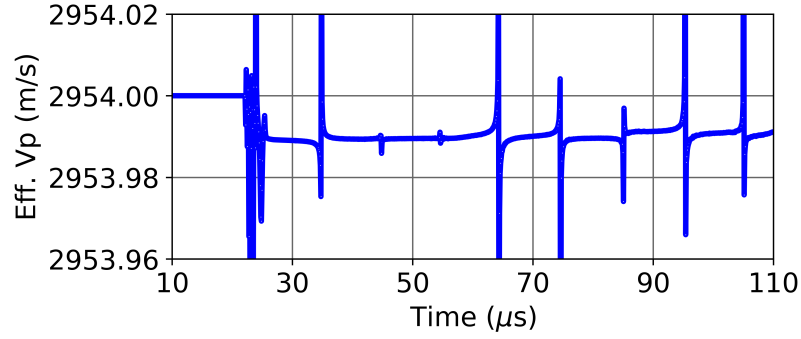

Figure 4.9: Effective P-wave velocity of the medium with vertical crack.

Figure 4.9 shows the effective P-wave velocity of the medium with a vertical crack. The results show minimal perturbations in the velocity compared to the one with horizontal crack in Figure 3.6 (b). Similarly, we get very small P-wave travel-time delay perturbations in Figure 4.10 for the vertical crack compared to the horizontal crack simulation results in Figure 4.4. Numerically, the reason behind the small

velocity perturbations is that now the normal crack compliance contributes to the P-wave velocity polarized along the direction (z or 2), but we calculate the effective P-wave velocity along the other direction (x or 1), which is the probe path. The probe direction is parallel to the crack as opposed to before when the probe direction was perpendicular to the crack. More on the side of the experimental point of view is discussed in the following chapter when we compare the results with other studies. Also, the trend shows that the delay is increasing and reaches its maximum around the time that the P-wave reaches the crack ($\approx$24 μs). This is because in this setup, the generated P-wave contributes to the opening and closing of the crack (our sources are not pure S-waves). However, if we rotate the crack in this source setup, this will not be the case because the P-wave particle motions will not be perpendicular to the crack surface.
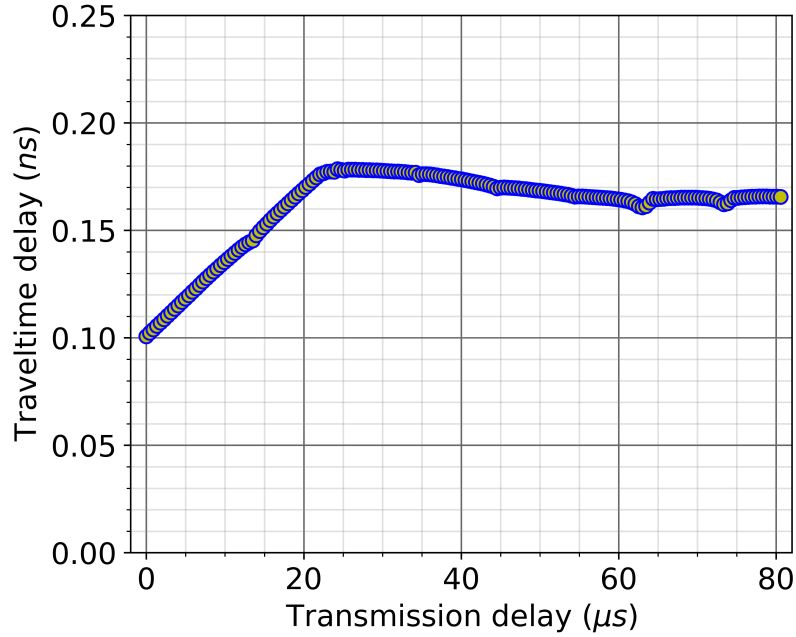

Figure 4.10: P-wave travel-time delay of the medium with vertical crack.

Chapter 5

Discussion, conclusions and future work

Rocks' microstructures such as cracks play a vital role in the observed nonlinearity, which is generally observed as a velocity change due to the changes in an applied force on a rock (e.g., Guyer and Johnson, 2009). TenCate et al. (2016) show some laboratory experiments in which they measure this velocity change phenomenon by perturbing the rock. Following these experiments, Rusmanugroho et al. (2020) use numerical modelling to better understand the phenomenon observed in the experimental study. In this study, we have shown some numerical examples to better understand the sorts of experiments used in Rusmanugroho et al. (2020)'s study. However, there are a few major differences, as stated in the previous chapters.

In this study, we have used the spectral element method as our numerical method for wave propagation simulations in a 2D problem. This choice allowed us to make unstructured mesh hence more realistic cracks shapes. We then needed to use an effective medium theory to average the medium. As mentioned by Rusmanugroho et al. (2020), the effective medium is often used for a static perturbation but is also

applicable in dynamic perturbations if the wavelength of the perturbation is larger than the crack aperture. Therefore, we used the linear slip effective medium to calculate the effective compliance tensor of the medium from which we calculated the effective velocity of the medium. After that, we calculated the P-wave travel-time delay using the effective P-wave velocity of the medium. In Chapter 3, we provided a detailed procedure for computing the P-wave travel-time delay. All the necessary steps are discussed with a few potential methods for performing the effective P-wave velocity calculations in that chapter. We discuss the results provided in Chapter 4 and compare them with other studies in the next few paragraphs.

In the first set of examples, we have shown the effect of the crack aperture on the effective P-wave velocity as well as the resulting travel-time delays. These examples show that with increasing the crack aperture, we have more velocity perturbations, and hence it produces higher travel-time delay. This is reasonable because the larger the crack aperture, the bigger the crack, so the larger the total displacement discontinuity. These results can be compared to the results of Rusmanugroho et al. (2020), where there are more cracks in the medium there is a larger travel-time delay in the medium than a single crack (i.e., to some extent more cracks are affecting the results in the same manner as fewer cracks with bigger aperture). This is related to the concept of the crack density in the medium. However, we cannot compare the amplitude of the results because of the methodological differences, but we can compare the trend, which is similar in both studies.

In the second set of examples in the results section, we tested the effect of crack filling velocity. The results show that the higher the difference between the background and the crack filling velocities, the higher the P-wave velocity perturbations and hence the higher the effective P-wave travel-time delay. We can explain this by the fact that the average velocity in a medium is smaller when we put a material (here a crack)

with a lower velocity. Also, a higher travel-time is expected by lowering the crack velocity because the wave travels slower in a crack with lower velocity.

In our final results, we showed the effect of crack orientation on the results. We see agreements with the experimental results of TenCate et al. (2016) and the numerical results of Rusmanugroho et al. (2020). Although we cannot compare the amplitude of the results with both studies for reasons such as the number of cracks and the dimensions, we see a decrease in the travel-time delay when the particle motion of the perturbing S-wave is parallel to the crack surface or bedding plane. When the particle motions are perpendicular to the crack surface or bedding plane, the amplitude of the travel-time delay is larger. This can be explained by displacement discontinuities, which are an indicator of the opening and closing of the crack. It is evident that with particle motions parallel to the crack surface or bedding plane, we have smaller opening and closing compared to when the particle motions are perpendicular to the bedding plane.

In all examples, we have seen that the displacement discontinuity or the clapping cracks play an essential rule in the travel-time delay observations. This supports that cracks are the major cause of the velocity change or the nonlinearity, as stated in other studies (e.g., Guyer and Johnson, 2009). Also, our results show that we are able to predict the cracks' orientations (horizontal or vertical) by comparing the P-wave travel-time delay results. Moreover, we are able to qualitatively predict the crack density in the medium; larger delay corresponds to larger crack density. It is hard to quantitatively estimate fracture clapping details by studying the oscillations associated with the travel-time delay in our results. This is because our results contain a wide range of frequencies, making it difficult to conclude. However, this is an interesting point to study more in the future. In general, our results show that the intact rock (without any defects or homogenous and isotropic rock) does not show

any velocity change, but in a cracked medium, we see perturbations in the P-wave velocity of the medium initiating when the wave reaches the crack. This agrees with Guyer and Johnson (1999), where they explain that the nonlinearity seen in real rocks is due to their small-scale structures (i.e., the rocks' bond system contains mechanical defects). Gardner et al. (1974) also state that the closing of cracks with pressure causes velocity perturbations in the rock. This result agrees with other studies done in the field in which they state that the stress change is one of the reasons for velocity change (e.g., Brenguier et al., 2008; Minato et al., 2012; Olivier et al., 2019). Although we have agreements with other studies, we suggest more studies to reach a clearer understanding of the phenomenon, as discussed below.

The first one is to solve one of our limitations in this study by implementing the linear slip theory into the SEM code. This allows us to have a better prediction of the displacement discontinuity and hence the clapping of the crack and make it more practical when placing a large number of cracks in the medium. The second suggestion is to modify the sources to be pure S-wave or P-wave sources. However, this is not something with high priority because if we consider the real situation of wave propagation in the Earth, it is the same as our sources that first the P-wave and then the S-wave propagates through the medium. A third possible study could be making a more realistic medium with more cracks and different orientations. Another important suggestion would be implementing the nonlinear wave equation in the SEM code so we can better predict the velocity change by taking the nonlinear parameters into account. It is worth mentioning that in our study using linear wave equation modelling, we see similar trends to those seen in the Rusmanugroho et al. (2020)'s study where they use nonlinear wave equation modelling. This leads us to conclude that the cracks are really completely dominating the results, with only a minor effect from the intrinsic nonlinearity of the material. One could also further

explore how much of this travel-time delay phenomenon is related to the nonlinear parameters as opposed to the linear parameters (compliances). In the end, it is worth mentioning that Rusmanugroho et al. (2020)'s study has not some of our limitations. Therefore one may use their method in which the nonlinear parameters and linear slip are implemented and included in the method for a better prediction of clapping crack and velocity change. However, it is fair to say that for getting results that are close to the experimental results of TenCate et al. (2016), more realistic crack shapes are needed. Therefore, our method is recommended if someone wants to have more realistic crack shapes and work on a 2D problem.

Bibliography

Aki, K., and P. G. Richards, 2002, Quantitative seismology.

Ali, A., 2011, Correlations between the effective permeability and seismic anisotropy of fractured reservoirs.

Bao, H., J. Bielak, O. Ghattas, L. F. Kallivokas, D. R. O'Hallaron, J. R. Shewchuk, and J. Xu, 1998, Large-scale simulation of elastic wave propagation in heterogeneous media on parallel computers: Computer methods in applied mechanics and engineering, **152**, 85–102.

Brenguier, F., M. Campillo, C. Hadziioannou, N. M. Shapiro, R. M. Nadeau, and E. Larose, 2008, Postseismic relaxation along the san andreas fault at parkfield from continuous seismological observations: science, **321**, 1478–1481.

Carcione, J. M., G. C. Herman, and A. Ten Kroode, 2002, Seismic modeling: Geophysics, **67**, 1304–1325.

Causon, D., and C. Mingham, 2010, Introductory finite difference methods for pdes: Bookboon.

Coates, R. T., and M. Schoenberg, 1995, Finite-difference modeling of faults and fractures: Geophysics, **60**, 1514–1526.

Fang, X., M. C. Fehler, Z. Zhu, Y. Zheng, and D. R. Burns, 2014, Reservoir fracture characterization from seismic scattered waves: Geophysical Journal International, **196**, 481–492.

Fang, X., Y. Zheng, and M. C. Fehler, 2017, Fracture clustering effect on amplitude variation with offset and azimuth analysesavoaz fracture characterization: Geophysics, **82**, N13–N25.

Gallot, T., A. Malcolm, T. L. Szabo, S. Brown, D. Burns, and M. Fehler, 2015, Characterizing the nonlinear interaction of s-and p-waves in a rock sample: Journal of Applied Physics, **117**, 034902.

Gao, K., E. Rougier, R. A. Guyer, Z. Lei, and P. A. Johnson, 2019, Simulation of crack induced nonlinear elasticity using the combined finite-discrete element method: Ultrasonics.

Gardner, G., L. Gardner, and A. Gregory, 1974, Formation velocity and density—the diagnostic basics for stratigraphic traps: Geophysics, **39**, 770–780.

Gharti, H., L. Langer, M. Roth, J. Tromp, U. Vaaland, and Z. Yan, 2017, Meshassist: an open-source and cross-platform meshing assistant tool.

Graves, R. W., 1996, Simulating seismic wave propagation in 3d elastic media using staggered-grid finite differences: Bulletin of the Seismological Society of America, **86**, 1091–1106.

Grechka, V., and M. Kachanov, 2006, Effective elasticity of fractured rocks: A snapshot of the work in progress: Geophysics, **71**, W45–W58.

Guo, J., T. Han, L.-Y. Fu, D. Xu, and X. Fang, 2019, Effective elastic properties of rocks with transversely isotropic background permeated by aligned penny-shaped cracks: Journal of Geophysical Research: Solid Earth, **124**, 400–424.

Guyer, R. A., and P. A. Johnson, 1999, Nonlinear mesoscopic elasticity: Evidence for a new class of materials: Physics today, **52**, 30–36.

——, 2009, Nonlinear mesoscopic elasticity: the complex behaviour of rocks, soil, concrete: John Wiley & Sons.

Hashin, Z., 1963, Theory of mechanical behavior of heterogeneous media: Techni-

cal report, TOWNE SCHOOL OF CIVIL AND MECHANICAL ENGINEERING PHILADELPHIA PA.

Haupert, S., G. Renaud, J. Rivière, and P. Shokouhi, 2019, Dynamic acousto-elastic testing, *in* Nonlinear Ultrasonic and Vibro-Acoustical Techniques for Nondestructive Evaluation: Springer, 509–546.

Helbig, K., 1998, A formalism for the consistent description of non-linear elasticity of anisotropic media: Revue de l'Institut Français du Pétrole, **53**, 693–708.

Hu, Y., and G. A. McMechan, 2009, Comparison of effective stiffness and compliance for characterizing cracked rocks: Geophysics, **74**, D49–D55.

Hudson, J., 1980, Overall properties of a cracked solid: Mathematical Proceedings of the Cambridge Philosophical Society, Cambridge University Press, 371–384.

——, 1994, Overall properties of a material with inclusions or cavities: Geophysical Journal International, **117**, 555–561.

Hudson, J. A., 1981, Wave speeds and attenuation of elastic waves in material containing cracks: Geophysical Journal International, **64**, 133–150.

Ikelle, L. T., and L. Amundsen, 2005, Introduction to petroleum seismology: Society of Exploration Geophysicists.

Jakobsen, M., J. A. Hudson, and T. A. Johansen, 2003a, T-matrix approach to shale acoustics: Geophysical Journal International, **154**, 533–558.

Jakobsen, M., T. A. Johansen, and C. McCann, 2003b, The acoustic signature of fluid flow in complex porous media: Journal of applied Geophysics, **54**, 219–246.

Johnson, P., and P. Rasolofosaon, 1996, Nonlinear elasticity and stress-induced anisotropy in rock: Journal of Geophysical Research: Solid Earth, **101**, 3113–3124.

Kachanov, M., 1992, Effective elastic properties of cracked solids: critical review of some basic concepts: Applied Mechanics Reviews, **45**, 304–335.

Kelly, K., R. Ward, S. Treitel, and R. Alford, 1976, Synthetic seismograms: A finite-

difference approach: Geophysics, **41**, 2–27.

Komatitsch, D., 1997, Méthodes spectrales et éléments spectraux pour l'équation de l'élastodynamique 2d et 3d en milieu hétérogène: PhD thesis.

Komatitsch, D., and J. Tromp, 1999, Introduction to the spectral element method for three-dimensional seismic wave propagation: Geophysical journal international, **139**, 806–822.

———, 2002, Spectral-element simulations of global seismic wave propagation—i. validation: Geophysical Journal International, **149**, 390–412.

Komatitsch, D., and J.-P. Vilotte, 1998, The spectral element method: an efficient tool to simulate the seismic response of 2d and 3d geological structures: Bulletin of the seismological society of America, **88**, 368–392.

Komatitsch, D., J.-P. Vilotte, R. Vai, J. M. Castillo-Covarrubias, and F. J. Sanchez-Sesma, 1999, The spectral element method for elastic wave equations: application to 2d and 3d seismic problems: Int. J. Numer. Meth. Engng., **45**, 1139–1164.

Martin, R., D. Komatitsch, C. Blitz, and N. Le Goff, 2008, Simulation of seismic wave propagation in an asteroid based upon an unstructured mpi spectral-element method: blocking and non-blocking communication strategies: International Conference on High Performance Computing for Computational Science, Springer, 350–363.

Meza-Fajardo, K. C., A. S. Papageorgiou, et al., 2008, The spectral element method (sem): formulation and implementation of the method for engineering seismology problems: Presented at the 14th World Conference on Earthquake Engineering (14WCEE).

Minato, S., T. Tsuji, S. Ohmi, and T. Matsuoka, 2012, Monitoring seismic velocity change caused by the 2011 tohoku-oki earthquake using ambient noise records: Geophysical Research Letters, **39**.

Nye, J., 1985, Physical properties of crystals: Their representation by tensors and matrices: Clarendon Press. Oxford science publications.

Olivier, G., F. Brenguier, R. Carey, P. Okubo, and C. Donaldson, 2019, Decrease in seismic velocity observed prior to the 2018 eruption of kīlauea volcano with ambient seismic noise interferometry: Geophysical Research Letters, **46**, 3734–3744.

Pecorari, C., 2015, Modeling non-collinear mixing by distributions of clapping microcracks: Wave Motion, **59**, 69–80.

Rasolofosaon, P. N., and H. Yin, 1996, Simultaneous characterization of anisotropy and nonlinearity in arbitrary elastic media-reflections on experimental data, *in* Seismic anisotropy: Society of Exploration Geophysicists, 141–179.

Rivière, J., G. Renaud, R. Guyer, and P. Johnson, 2013, Pump and probe waves in dynamic acousto-elasticity: Comprehensive description and comparison with nonlinear elastic theories: Journal of applied physics, **114**, 054905.

Rüger, A., 1998, Variation of p-wave reflectivity with offset and azimuth in anisotropic media: Geophysics, **63**, 935–947.

Rusmanugroho, H., A. Malcolm, and M. Darijani, 2020, A numerical model for the nonlinear interaction of elastic waves with cracks: Wave Motion, **92**, 102444.

Rusmanugroho, H., and G. A. McMechan, 2010, Modeling sensitivity of 3d, 9-c wide azimuth data to changes in fluid content and crack density in cracked reservoirs: Geophysics, **75**, T155–T165.

——, 2012, 3d, 9c seismic modeling and inversion of weyburn field data: Geophysics, **77**, R161–R173.

Schoenberg, M., 1980, Elastic wave behavior across linear slip interfaces: The Journal of the Acoustical Society of America, **68**, 1516–1521.

Schoenberg, M., and J. Douma, 1988, Elastic wave propagation in media with parallel fractures and aligned cracks: Geophysical prospecting, **36**, 571–590.

Schoenberg, M., and C. M. Sayers, 1995, Seismic anisotropy of fractured rock: Geophysics, **60**, 204–211.

Schuberth, B., 2003, The spectral element method for seismic wave propagation: PhD thesis, Master's thesis, Ludwigs-Maximilians-Universität Munchen.

Slawinski, M. A., 2010, Waves and rays in elastic continua: World Scientific.

Stein, S., and M. Wysession, 2009, An introduction to seismology, earthquakes, and earth structure: John Wiley & Sons.

Tarantola, A., 1986, A strategy for nonlinear elastic inversion of seismic reflection data: Geophysics, **51**, 1893–1903.

TenCate, J., A. Malcolm, X. Feng, and M. Fehler, 2016, The effect of crack orientation on the nonlinear interaction of a p wave with an s wave: Geophysical Research Letters, **43**, 6146–6152.

Tessmer, E., 1995, 3-d seismic modelling of general material anisotropy in the presence of the free surface by a chebyshev spectral method: Geophysical Journal International, **121**, 557–575.

Thomsen, L., 1986, Weak elastic anisotropy: Geophysics, **51**, 1954–1966.

Vetri, L., E. Loinger, J. Gaiser, A. Grandi, and H. Lynn, 2003, 3d/4c emilio: Azimuth processing and anisotropy analysis in a fractured carbonate reservoir: The Leading Edge, **22**, 675–679.

Virieux, J., 1986, P-sv wave propagation in heterogeneous media: Velocity-stress finite-difference method: Geophysics, **51**, 889–901.

Wang, X., 2015, Numerical modeling of seismic wave propagation in underground mines.: PhD thesis, Laurentian University of Sudbury.

Wang, Y., H. Takenaka, and T. Furumura, 2001, Modelling seismic wave propagation in a two dimensional cylindrical whole earth model using the pseudospectral method: Geophysical Journal International, **145**, 689–708.

Xu, Z. J., and X. Song, 2009, Temporal changes of surface wave velocity associated with major sumatra earthquakes from ambient noise correlation: Proceedings of the National Academy of Sciences, **106**, 14207–14212.

Zhao, L., 2014, Poroelastic and seismic characterization of heterogeneous reservoir rocks: PhD thesis.

Zhao, L., Q. Yao, D.-H. Han, F. Yan, and M. Nasser, 2016, Characterizing the effect of elastic interactions on the effective elastic properties of porous, cracked rocks: Geophysical Prospecting, **64**, 157–169.

Zheng, Y., X. Fang, M. C. Fehler, and D. R. Burns, 2013, Seismic characterization of fractured reservoirs by focusing gaussian beams: Geophysics, **78**, A23–A28.

Appendix A

Some derivations

In this appendix, we show how to derive Equations (2.59) and (2.60) for averaging the stress and strain on a surface based on boundary elements by expanding Equation (2.58) from Section 2.6.2.

A.1 Formula for averaging surface

After plugging Equations (2.55), (2.57) into (2.58) we have,

$$
\begin{aligned}
\langle \varepsilon_{ij} \rangle &= \frac{1}{2S} \int_l (\varepsilon_{ik} x_k n_j + \varepsilon_{jk} x_k n_i) dl, \\
\langle \sigma_{ij} \rangle &= \frac{1}{2S} \int_l (\sigma_{ik} n_k x_j + \sigma_{jk} n_k x_i) dl.
\end{aligned}
\tag{A.1}
$$

Expanding Equation (A.1) into each element gives,

$$
\begin{aligned}
\langle \varepsilon_{11} \rangle &= \frac{1}{2S} \int_l (\varepsilon_{1k} x_k n_1 + \varepsilon_{1k} x_k n_1) dl \\
&= \frac{1}{S} \int_l (\varepsilon_{1k} x_k n_1) dl, \\
\langle \varepsilon_{22} \rangle &= \frac{1}{2S} \int_l (\varepsilon_{2k} x_k n_2 + \varepsilon_{2k} x_k n_2) dl \\
&= \frac{1}{S} \int_l (\varepsilon_{2k} x_k n_2) dl, \\
\langle \varepsilon_{12} \rangle &= \frac{1}{2S} \int_l (\varepsilon_{1k} x_k n_2 + \varepsilon_{2k} x_k n_1) dl,
\end{aligned}
\tag{A.2}
$$

and,

$$
\begin{aligned}
\langle \sigma_{11} \rangle &= \frac{1}{2S} \int_l (\sigma_{1k} n_k x_1 + \sigma_{1k} n_k x_1) dl \\
&= \frac{1}{S} \int_l (\sigma_{1k} n_k x_1) dl, \\
\langle \sigma_{22} \rangle &= \frac{1}{2S} \int_l (\sigma_{2k} n_k x_2 + \sigma_{2k} n_k x_2) dl \\
&= \frac{1}{S} \int_l (\sigma_{2k} n_k x_2) dl, \\
\langle \sigma_{12} \rangle &= \frac{1}{2S} \int_l (\sigma_{1k} n_k x_2 + \sigma_{2k} n_k x_1) dl.
\end{aligned}
\tag{A.3}
$$

Based on Figure 2.2, which shows our surface of interest with four boundaries, we could write Equation A.3 for each surface boundary as follows,

$$
\begin{aligned}
\langle \varepsilon_{11} \rangle &= \frac{1}{S} \Big[\int_{l_1} (\varepsilon_{11} x_1 n_1 + (\varepsilon_{12} x_2 n_1) dl_1 + \int_{l_2} (\varepsilon_{11} x_1 n_1 + \varepsilon_{12} x_2 n_1) dl_2 + \\
&\quad \int_{l_3} (\varepsilon_{11} x_1 n_1 + \varepsilon_{12} x_2 n_1) dl_3 + \int_{l_4} (\varepsilon_{11} x_1 n_1 + \varepsilon_{12} x_2 n_1) dl_4 \Big], \\
\langle \varepsilon_{22} \rangle &= \frac{1}{S} \Big[\int_{l_1} (\varepsilon_{21} x_1 n_2 + \varepsilon_{22} x_2 n_2) dl_1 + \int_{l_2} (\varepsilon_{21} x_1 n_2 + \varepsilon_{22} x_2 n_2) dl_2 + \\
&\quad \int_{l_3} (\varepsilon_{21} x_1 n_2 + \varepsilon_{22} x_2 n_2) dl_3 + \int_{l_4} (\varepsilon_{21} x_1 n_2 + \varepsilon_{22} x_2 n_2) dl_4 \Big], \\
\langle \varepsilon_{12} \rangle &= \frac{1}{2S} \Big[\int_{l_1} (\varepsilon_{11} x_1 n_2 + \varepsilon_{12} x_2 n_2 + \varepsilon_{21} x_1 n_1 + \varepsilon_{22} x_2 n_1) dl_1 + \\
&\quad \int_{l_2} (\varepsilon_{11} x_1 n_2 + \varepsilon_{12} x_2 n_2 + \varepsilon_{21} x_1 n_1 + \varepsilon_{22} x_2 n_1) dl_2 + \\
&\quad \int_{l_3} (\varepsilon_{11} x_1 n_2 + \varepsilon_{12} x_2 n_2 + \varepsilon_{21} x_1 n_1 + \varepsilon_{22} x_2 n_1) dl_3 + \\
&\quad \int_{l_4} (\varepsilon_{11} x_1 n_2 + \varepsilon_{12} x_2 n_2 + \varepsilon_{21} x_1 n_1 + \varepsilon_{22} x_2 n_1) dl_4 \Big],
\end{aligned}
\tag{A.4}
$$

and,

$$
\begin{aligned}
\langle\sigma_{11}\rangle =\ & \frac{1}{S}\Bigg[\int_{l_1}(\sigma_{11}n_1x_1+\sigma_{12}n_2x_1)dl_1+\int_{l_2}(\sigma_{11}n_1x_1+\sigma_{12}n_2x_1)dl_2+\\
& \int_{l_3}(\sigma_{11}n_1x_1+\sigma_{12}n_2x_1)dl_3+\int_{l_4}(\sigma_{11}n_1x_1+\sigma_{12}n_2x_1)dl_4\Bigg],\\
\langle\sigma_{22}\rangle =\ & \frac{1}{S}\Bigg[\int_{l_1}(\sigma_{21}n_1x_2+\sigma_{22}n_2x_2)dl_1+\int_{l_2}(\sigma_{21}n_1x_2+\sigma_{22}n_2x_2)dl_2+\\
& \int_{l_3}(\sigma_{21}n_1x_2+\sigma_{22}n_2x_2)dl_3+\int_{l_4}(\sigma_{21}n_1x_2+\sigma_{22}n_2x_2)dl_4\Bigg],\\
\langle\sigma_{12}\rangle =\ & \frac{1}{2S}\Bigg[\int_{l_1}(\sigma_{11}n_1x_2+\sigma_{12}n_2x_2+\sigma_{21}n_1x_1+\sigma_{22}n_2x_1+)dl_1+\\
& \int_{l_2}(\sigma_{11}n_1x_2+\sigma_{12}n_2x_2+\sigma_{21}n_1x_1+\sigma_{22}n_2x_1+)dl_2+\\
& \int_{l_3}(\sigma_{11}n_1x_2+\sigma_{12}n_2x_2+\sigma_{21}n_1x_1+\sigma_{22}n_2x_1+)dl_3+\\
& \int_{l_4}(\sigma_{11}n_1x_2+\sigma_{12}n_2x_2+\sigma_{21}n_1x_1+\sigma_{22}n_2x_1+)dl_4\Bigg].
\end{aligned}
\tag{A.5}
$$

After we substitute the elements of n we get the final Equations (2.59) and (2.60).

Appendix B

Code validations

In this appendix, we validate the accuracy of the codes we use in our study. In the following sections, three main codes are validated: the SEM, the effective P-wave velocity, and the travel-time delay codes.

B.1   Wave simulation based on SEM

We validate the open-source code, <u>SPECFEM2D</u>, by two methods. First, we compare the radiation patterns of a diffraction point in an elastic medium and compare it with analytical solutions. Then, we compare the P-wave reflection coefficients from the numerical examples with analytical solutions.

B.1.1   Radiation Patterns

In this section, we provide the analytical solutions of radiation patterns in an elastic medium and then compare it with our numerical simulations. Figure B.1 shows all types of waves and their conversion possibilities. Note that there is no conversion between the SH-wave to the other two and vice versa.

Figure B.1: All possible types of diffraction waves are shown. The first wave is the incident wave, and the second wave is the diffracted wave (i.e., columns and rows correspond to the incident and diffracted P-, SV- and SH-waves, respectively). The arrows indicate the first displacement of the incident wave. Also, there is no conversion between the SH-wave to the P- and SV-waves and vice versa. The plot is adopted from Tarantola (1986).

The analytical solutions are shown in Figures B.2a, B.2b and B.2c for P-wave velocity, S-wave velocity and density (ρ) perturbations, respectively. The corresponding numerical examples are shown in Figures B.2d, B.2e and B.2f, respectively. In our case, P-wave is the incident wave. Therefore, we only consider the left columns of the analytical solutions to compare with our numerical scattered wavefields (see, also Figure B.1). We see that the numerical results are in agreement with the analytical solutions.
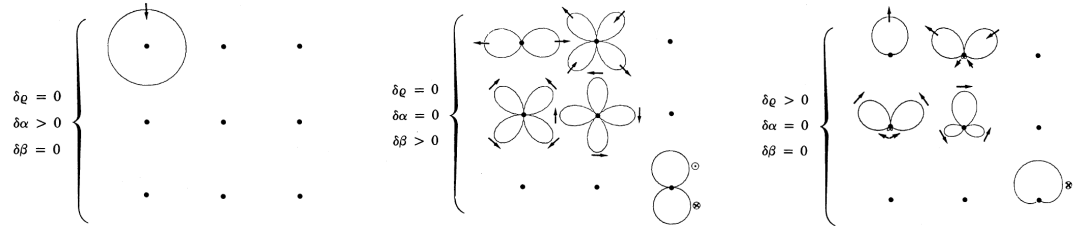
(a) Diffracted waves with a P-wave velocity perturbation

(b) Diffracted waves with an S-wave velocity perturbation

(c) Diffracted waves with a ρ perturbation

75
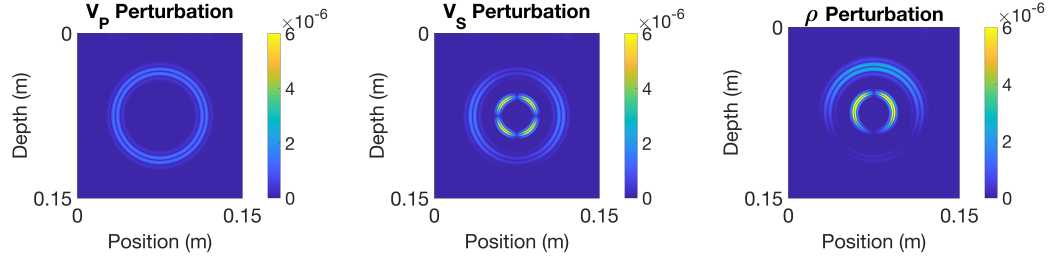
(d) P-wave velocity diffractor of a 500 m/s difference from the background

(e) S-wave velocity diffractor of a 500 m/s difference from the background

(f) ρ diffractor of a 500 kg/m^3 difference from the background

Figure B.2: (a), (b), and (c) are the analytical solutions of the radiation patterns for the P-wave, S-wave and density (ρ) perturbations in a medium, respectively. The incident and diffracted waves are as in Figure B.1. The arrows indicate the first displacement of the diffracted waves. These plots are also adopted from Tarantola (1986). The corresponding numerical scattered wavefields for P-wave incidents are shown in (d), (e), and (f).

B.1.2 Reflection coefficients

In this section, the P-wave reflection coefficients of a reflection boundary in a two-layered medium are presented. The size of the medium is 3 km $\times$ 1 km. The elastic properties of the top layer are $V_P = 2000$ m/s, $V_S = 750$ m/s and $\rho = 2000$ kg/m^3, and for the bottom layer are $V_P = 4000$ m/s, $V_S = 1500$ m/s and $\rho = 2500$ kg/m^3. The analytical solutions are calculated from the Zeoppritz equations (e.g., Aki and Richards, 2002). For the numerical simulations, we have the same model with 500000 elements using 116 receivers with 25 m spacing at the surface. Figure B.3 shows that the agreement between the analytical solutions and the numerical simulations is increased by getting closer to the assumption of incident plane wave used by Zeoppritz. This happens when we increase the first layer depth and also when we increase the frequency of our sources.

P-wave reflectivity
Source frequency = 25 Hz
Top layer thickness = 200 m

(a)

P-wave reflectivity
Source frequency = 75 Hz
Top layer thickness = 200 m

(b)

P-wave reflectivity
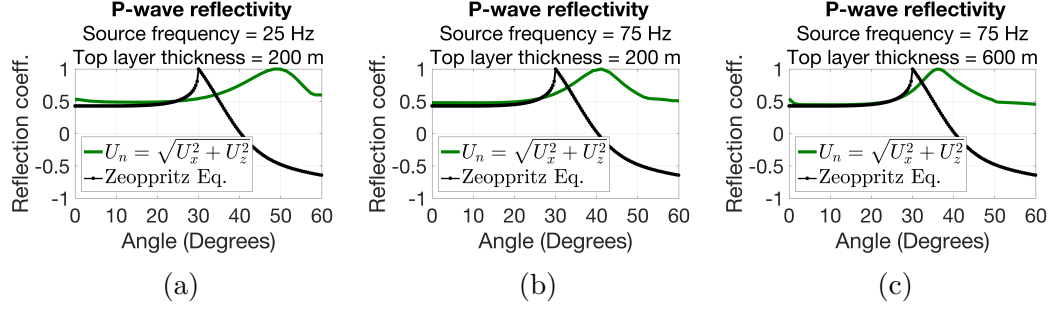Source frequency = 75 Hz
Top layer thickness = 600 m

(c)

Figure B.3: P-wave reflection coefficients are improved by increasing the frequency and the top layer thickness. The error between the Zeoppritz equations and $U_n = \sqrt{U_x{}^2 + U_z{}^2}$ from the numerical simulations, at 10.6°, is (a) 13.8%, (b) 11.3%, and (c) 4.3%. Error decreases by approaching the plane wave source assumption used by Zeoppritz, which, in our case, is increasing the depth of the interface or increasing the frequency.

B.2 Effective P-wave calculations

From Figures 3.4 and 3.6, we see that when the displacement discontinuity is equal to zero, there are no velocity perturbations, and we get the effective velocity equal to the background P-wave velocity. This shows the accuracy of our code using the crack compliance matrix method. For another method, using the stress and strain relationship, we see that when the wave does not hit the crack, the effective velocity of the medium is the same as the background velocity (see Figure 3.3). This also indicates the validity of the employed code.

B.3 Travel-time delay calculations

In this section, we check the validity of the travel-time delay code. Figure B.4a shows a medium with a constant effective velocity of 3000 m/s, which has the same velocity as its un-cracked medium. Figure B.4b shows its corresponding travel-time delay, which is expected to be zero. Our results show a very small number close to zero.
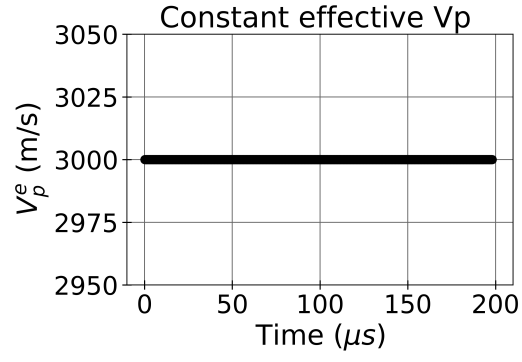
(a) Constant effective velocity
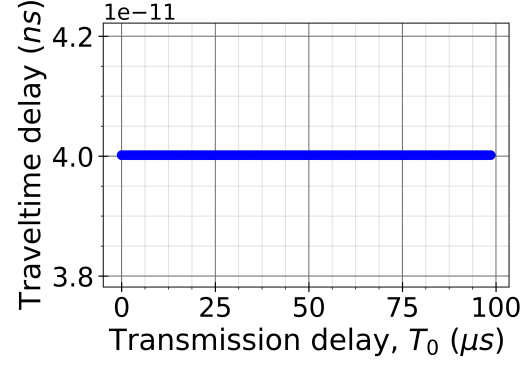
(b) Corresponding travel-time delay of the medium shown in (a)

Figure B.4: The constant effective velocity is the same as the velocity of a medium without any crack; therefore, zero travel-time delay is expected.